Correspondence to:
Q. Libois,
quentin.libois@meteo.fr

Uncertainty of SW Cloud Radiative Effect in Atmospheric Models Due to the Parameterization of Liquid Cloud Optical Properties

E. Jahangir[1], Q. Libois[1] ⓘ, F. Couvreux[1] ⓘ, B. Vié[1] ⓘ, and D. Saint-Martin[1] ⓘ

[1]CNRM, Université de Toulouse, Météo-France, CNRS, Toulouse, France

Abstract Clouds are largely responsible for the spread of climate models predictions. Here we focus on the uncertainties in cloud shortwave radiative effect due to the parameterization of liquid cloud single scattering properties (SSPs) from liquid water content (LWC) and droplet number concentration (N), named parameterization of cloud optical properties. Uncertainties arise from not accounting for the droplet size distribution (DSD)—which affects the estimation of the effective radius (r_{eff}) and modulates the r_{eff}-dependency of the SSPs—and from averaging SSPs over wide spectral bands. To assess these uncertainties a series of r_{eff}-dependent SSPs parameterizations corresponding to various DSDs and spectral averaging methods are derived and implemented in a radiative code. Combined with the DSD-dependent estimation of r_{eff} they are used to compute the bulk radiative properties (reflectance, transmittance, absorptance) of various clouds (defined in terms of LWC and N), including a homogeneous cloud, more realistic case studies, and outputs of a climate model. The results show that the cloud radiative forcing can vary up to 20% depending on the assumed DSD. Likewise, differences up to 20% are obtained for heating rates. The estimation of r_{eff} is the main source of uncertainty, while the SSPs parameterization contributes to around 20% of the total uncertainty. Spectral averaging is less an issue, except for atmospheric absorption. Overall, global shortwave cloud radiative effect can vary by 6 W m^{-2} depending on the assumed DSD shape, which is about 13% of the best observational estimate.

Plain Language Summary Climate predictions differ a lot from one model to another, and the difficulty to simulate how clouds will behave in a warmer world is largely responsible for that. The radiative effect of clouds depends on the size of the individual droplets forming a cloud, a quantity that is not explicitly represented in climate models. In this study we investigate how not accounting for the detailed droplet size distribution affects the capability of climate models to reliably predict the radiative effect of clouds. By assuming a variety of droplet size distributions in a set of simulations, we observe that apparently similar clouds in climate models can have very different radiative impacts depending on the assumed distribution. This is primarily attributed to the estimation of the effective radius of cloud droplets, a key quantity that drives cloud radiative properties. Differences up to 20% are observed on critical quantities such as fluxes at top-of-atmosphere and at the surface. The absorption of radiation within clouds is also significantly altered. The impact on the global estimate of shortwave cloud radiative effect is around 13%, which highlights the need to improve the representation of the microphysical characteristics of clouds to run more reliable climate predictions.

1. Introduction

The Earth radiative budget, which is the primary driver of Earth's climate, is largely governed by clouds, whose response to global warming remains the largest source of uncertainty in the estimation of the effective climate sensitivity (the change in near-surface temperature resulting from CO_2 doubling) by state-of-the-art general circulation models (GCMs) (Zelinka et al., 2020). In the shortwave (SW), clouds tend to cool the Earth by reflecting solar radiation. On the contrary, clouds trap longwave (LW) radiation emitted by the surface, which tends to warm the system. The cloud radiative effect (CRE, Charlock & Ramanathan, 1985), defined as the difference between net radiative fluxes in cloudy and clear-sky conditions (either at the top of atmosphere [TOA] or at the surface), quantifies these counteracting cooling and warming effects. The best estimations from a combination of satellite (Loeb et al., 2018) and ground measurements (Wild et al., 2019) suggest that CRE is about −47.7 W m^{-2} in the SW at TOA (−56 W m^{-2} at the surface) and 28 W m^{-2} (both at TOA and at the surface) in the LW, meaning that

clouds overall cool the system. Although in average GCMs reproduce these observations well, significant differences exist among the CRE simulated by 38 individual GCMs participating in the sixth phase of the Coupled Model Intercomparison Project (CMIP6) as reported by Wild (2020). Indeed, the SW CRE at TOA ranges from −41 to −60 W m^{-2} (−43 to −63 W m^{-2} at the surface) while the LW CRE at TOA ranges from 19 to 29 W m^{-2} (22 to 30 W m^{-2} at the surface). This points to the long-standing difficulty to simulate clouds and their radiative effect, and makes questionable the capability of GCMs to predict how CRE might be altered in a warmer climate.

Several factors can explain these inter-model discrepancies: differences in total cloud fraction (Nam et al., 2012; Vignesh et al., 2020), location of the clouds, diurnal or seasonal cycles of the clouds, cloud optical properties (Engström et al., 2014; Hu & Stamnes, 2000), radiative treatment of cloudy layers (Costa & Shine, 2006; Pincus et al., 2003) or even surface albedo (Hourdin et al., 2013). Although there are many reasons for clouds to differ amongst GCMs, due to differences in the physical parameterizations trying to catch the complex and unresolved physical processes of cloud formation and evolution, it is worth pointing out that even with identical clouds (same spatial distribution, cloud fraction, amount of condensate etc.), distinct GCMs may predict distinct CRE. This stems from the fact that CRE fundamentally depends on the way cloudy layers are treated in the radiative scheme of each model (e.g., Fouquart et al., 1991), and how their bulk radiative properties—namely transmittance, reflectance and absorptance—are computed.

Generally GCMs rely on one-moment microphysical schemes, meaning that only the hydrometeors water contents (liquid, ice, rain, snow etc.) are prognostic variables. It implies that the number concentration N of cloud particles, and consequently the effective radius r_{eff} of the hydrometeors (the ratio of the third moment to the second moment of the particle size distribution), are simply diagnosed from the liquid water content (LWC) and ice water content (IWC) (most often along with a prognostic aerosols mass concentration (e.g., Boucher & Lohmann, 1995). Hence radiative transfer schemes in GCMs essentially take as inputs vertical profiles of LWC, IWC, cloud fraction, and aerosol concentration, and rely on a succession of assumptions to compute radiative fluxes based on this limited information. In addition, for computation cost reasons, the radiative calculations are performed in a limited number of spectral bands, in which the single scattering properties (SSPs) of clouds are considered constant. This number can range from a single one (Geleyn et al., 2017) to a dozen (as in the Rapid Radiative Transfer Model for General Circulation Models Applications [RRTMG; Clough et al., 2005], which is implemented in several GCMs). Computing the bulk radiative properties of clouds thus requires two preliminary steps: (a) treating the vertical overlap of cloud layers and their subgrid horizontal and vertical heterogeneities; (b) parameterizing cloud optical properties for given LWC and IWC. The latter generally includes the parameterization of r_{eff} on the one hand, and the computation of the band-averaged cloud SSPs—that is, the fundamental quantities describing the optical characteristics of a cloudy layer, which are detailed below—on the other hand. The question of cloud overlap has been the focus of many research studies (Di Giuseppe & Tompkins, 2015; Geleyn et al., 1979; Hogan & Illingworth, 2000; Räisänen et al., 2004; Sulak et al., 2020). Subgrid heterogeneities have also been extensively investigated over the past 20 years (Barker et al., 2002; Jouhaud et al., 2018; Pincus et al., 2005; Shonk & Hogan, 2008), including their effects on the intensity of subgrid 3D radiative effects (Barker et al., 2016; Hogan et al., 2016). Regarding cloud SSPs, most recent studies focused on the ice clouds (Edwards et al., 2007; Baum et al., 2011; Yang et al., 2013; W. Zhao et al., 2018), probably because clouds made of spherical droplets have been considered as largely understood. The parameterization of liquid cloud SSPs has indeed received limited attention since the seminal works of Fouquart and Bonnel (1980), Stephens (1978) and Slingo and Schrecker (1982), although the choice of these SSPs has been shown to alter CRE computations (Fouquart et al., 1991; Freidenreich & Ramaswamy, 2005). This impact is much stronger in the SW than in the LW, because multiple scattering makes the bulk radiative properties very sensitive to SSPs. For the aforementioned reasons the present study only tackles the SW radiative properties of liquid clouds.

The interactions of spherical cloud particles with solar radiation is well described by the Lorenz-Mie theory (Van De Hulst, 1968), which applies to particles comparable in size to the wavelength of incident radiation. This theory provides the SSPs of a spherical particle, in particular the extinction efficiency Q_{ext}, the asymmetry parameter g, and the single scattering albedo ω. Q_{ext} determines the fraction of the geometrical cross sectional area that contributes to light extinction. g is the average cosine of the deviation angle of the scattering phase function, the latter describing the angular distribution of scattered light. g is used here instead of the full scattering phase function, because most GCMs rely on two-stream radiative transfer codes which only use g (Fouquart & Bonnel, 1980; Meador & Weaver, 1980). ω quantifies the contribution of scattering to the total extinction. The single scattering

co-albedo 1-ω hence quantifies the contribution of absorption. These SSPs depend on the size of the particles, on the wavelength of incident radiation and on the refractive index of liquid water.

To compute cloud SSPs on given spectral bands, SSPs of individual droplets must be averaged over the cloud droplet size distribution (DSD) and across the spectral bands. Because SSPs strongly vary with droplet size and incident wavelength, and since the DSD is not resolved in a GCM simulation, computing these averages is not straightforward. This has given rise to a variety of parameterizations, generally giving the SSPs for individual spectral bands as a function of r_{eff}. These parameterizations implicitly assume a specific DSD. They also treat in different ways the spectral averaging issue. While g and Q_{ext} barely vary within spectral bands, the co-albedo (1-ω) can show significant variations (up to 100%) in a single band (Dobbie et al., 1999). Since the relationships between bulk radiative properties and the SSPs are highly nonlinear, using linear averages of 1-ω on each spectral band can lead to biases in bulk radiative properties. This issue was tackled with a variety of strategies, most of which aiming at minimizing the errors in flux computations (Chou et al., 1998; Edwards & Slingo, 1996; Espinoza, 1996; Räisänen, 1999). This stresses that spectral averaging has to be carefully considered when attempting to derive new SSPs parameterizations.

In practice, many parameterizations currently used in atmospheric models date back to the 80's and 90's (Edwards & Slingo, 1996; Fouquart, 1988; Slingo & Schrecker, 1982; Stephens, 1978). They are used for instance in the radiative codes available in the Weather Research and Forecasting (WRF) model (Chou et al., 1998; Dudhia, 1989), in the Hadley Centre (Pope et al., 2000) and IPSL (Madeleine et al., 2020) climate models, and in the radiative scheme of the Integrated Forecasting System (Hogan & Bozzo, 2018; Manners, 2015). However, Nielsen et al. (2014) recently pointed out that using the parameterizations from Fouquart (1988) and Slingo and Schrecker (1982) can generate large biases compared to detailed Lorenz-Mie computations. This highlights the need for revisiting the parameterization of SSPs.

The estimation of r_{eff} from LWC also depends on an assumption on the DSD (Martin et al., 1994). In most cases, this underlying assumption is inconsistent with that used to derive the r_{eff} dependent SSPs, although generally none is explicit. For instance Slingo and Schrecker (1982) mention seven different DSDs used to derive their parameterization, but no details are revealed about how SSPs are averaged over these seven DSDs. This also holds for the parameterization of Hu and Stamnes (1993), who in addition use SSPs computed at specific wavelengths rather than averaged over bands. This same study concluded that the impact of DSD shape on SSPs could not exceed 6%, which was cited in subsequent studies as a reason not to focus too much on the DSD. However SSPs were only computed for a cloud with effective radius of 20 μm, and the differences in SSPs were not translated into errors in bulk radiative properties. In the present study, the DSD assumptions used for estimating r_{eff} and the SSPs, along with the spectral averaging, will be clearly stated.

The overarching objective of this paper is thus to estimate the uncertainties on CRE resulting from the assumption on the DSD and the spectral averaging strategy. To this end, a large set of SSPs parameterizations is developed, based on detailed Lorenz-Mie computations applied to well-defined DSDs, and various spectral averaging methods are used. These new parameterizations are meant to be made available to the community, to be used in place of the historical ones which can hardly be traced back to actual DSDs. These parameterizations are implemented in the radiative transfer code ecRad (Hogan & Bozzo, 2018) and combined to a consistent r_{eff} estimation to assess the overall impact of these choices on the simulated CRE. This sensitivity study is performed for several single column case studies of clouds, as well as for global outputs of a climate model. The paper is partitioned as follows. Section 2 provides complementary details about the DSD and spectral averaging issues. Section 3 describes how the parameterizations are derived and Section 4 shows the application of the newly developed parameterizations on cloudy atmospheres. These results are discussed along with perspectives in Section 5.

2. Theoretical Background

In this section we detail how the shape of the DSD affects the relationship between LWC and r_{eff}, and present the two types of DSDs used in this paper to represent clouds. In addition, preliminary ecRad simulations are performed to demonstrate that changing cloud SSPs parameterization in a radiative transfer code can make a difference in terms of the CRE. This is what initially motivated the present study.
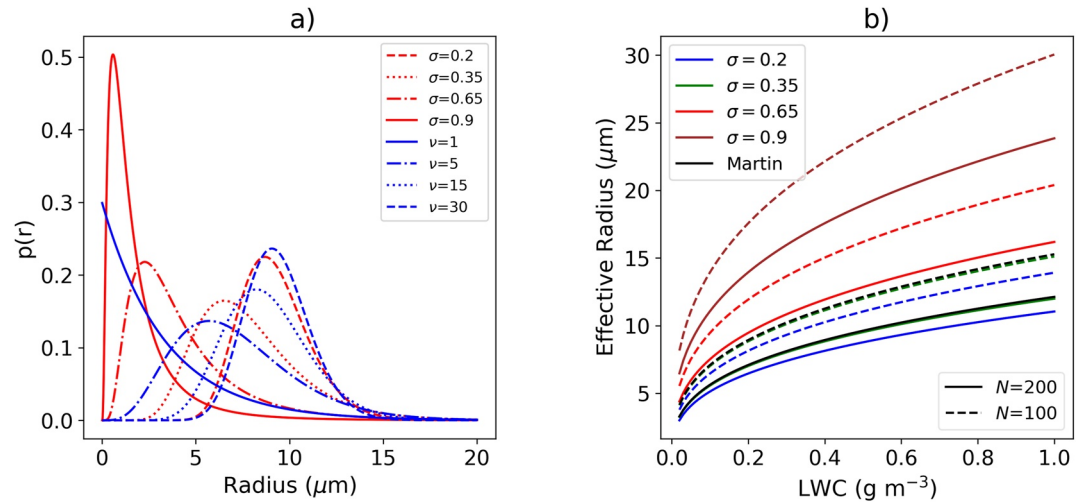
Figure 1. (a) Lognormal and modified gamma functions for different shape parameters (σ and ν correspond to the lognormal and modified gamma functions, respectively) but similar r_{eff} of 10 μm. (b) r_{eff}-LWC relation derived for 4 lognormal distributions from Equation 5. The solid lines correspond to $N = 200$ cm^{-3} and the dashed lines to $N = 100$ cm^{-3}. The curves labeled *Martin* were obtained using the value $k = 0.67$, as recommended by Martin et al. (1994).

2.1. Parameterization of Cloud Optical Properties

Let us consider $n(r)$, the cloud droplet number concentration per unit of cloud droplet radius r, hereafter called DSD. The total number concentration N is defined as:

$$N = \int_0^\infty n(r) \mathrm{d}r. \tag{1}$$

LWC is proportional to the third moment of the DSD:

$$\text{LWC} = \frac{4}{3} \pi \rho_w N \int_0^\infty r^3 p(r) \mathrm{d}r, \tag{2}$$

where $p(r) = n(r)/N$ is the normalized DSD and ρ_w is the density of liquid water. The modified gamma and lognormal distributions are commonly used to describe clouds DSD (Geoffroy et al., 2010; Misumi et al., 2018; C. Zhao et al., 2006). In this paper the following forms adapted from Miles et al. (2000) are used:

$$p(r) = \frac{1}{\sqrt{2\pi}\sigma r} \exp\left(\frac{-(\ln(r/r_n))^2}{2\sigma^2}\right), \quad \text{for lognormal,} \tag{3}$$

$$p(r) = \frac{1}{\Gamma(\nu)} \left(\frac{r}{r_n}\right)^{\nu-1} \frac{1}{r_n} \exp\left(-\frac{r}{r_n}\right), \quad \text{for modified gamma,} \tag{4}$$

where r_n is the median droplet radius in Equation 3 and a nonphysical scaling radius in Equation 4, and Γ is the gamma function. σ and ν are hereafter referred as shape parameters. Figure 1a shows these functions for various shape parameters but with a fixed r_{eff} of 10 μm. It highlights that distributions with identical r_{eff} can be practically very different. For these two DSDs, r_{eff} can be explicitly computed as a function of N and LWC. It takes the following form:

$$r_{\text{eff}} = \left(\frac{1}{k}\right)^{1/3} \left(\frac{3\text{LWC}}{4\rho_w \pi N}\right)^{1/3}, \tag{5}$$

where expressions for the parameter k are provided in Table 1. Hence k only depends on the shape parameters σ or ν. Interestingly, Martin et al. (1994) found a similar relationship between r_{eff} and LWC based on *in situ* observations in stratocumuli, and identified distinct k values for clouds over ocean and over land. They

Table 1
Expressions of k for the Lognormal and Modified Gamma Distributions, in Terms of the Shape Parameters σ and ν

Distribution function	k	r_{eff}
Lognormal	$e^{-3\sigma^2}$	$r_n e^{\frac{3}{2}\sigma^2}$
Modified gamma	$\frac{(\nu^2+\nu)}{(\nu+2)^2}$	$r_n(\nu+2)$

recommend to use $k = 0.67$ over land, and $k = 0.80$ over ocean, which remain widely used values.

LWC and N are the usual variables provided to the radiative scheme. However Equation 5 highlights that an additional shape parameter is needed to compute r_{eff}. Figure 1b shows how r_{eff} varies with LWC for distinct lognormal distributions for N equal to 100 and 200 cm^{-3}. σ varies from 0.2 to 0.9, which covers the field observations reported in Miles et al. (2000). A factor larger than two in r_{eff} is found for these extreme values, which correspond to k values of 0.88 and 0.09, respectively. Thus, neglecting the impact of the shape parameter on the effective radius results in an uncertainty, called r_{eff}-*uncertainty* hereafter. When k is not provided to the radiative scheme, the r_{eff}-uncertainty impacts the overall estimation of SSPs, and consequently alters the cloud bulk radiative properties.

r_{eff} has long been identified as the driving quantity for cloud SSPs since it is related to the volume-to-surface-area ratio of liquid droplets, a quantity that compares absorption (which occurs in the volume) and scattering (which occurs at the surface) and naturally arises in the derivation of single scattering albedo (Grenfell & Warren, 1999; Mitchell, 2002). However r_{eff} does not contain any information about the shape of the DSD. For instance, based on aircraft observations, Brenguier et al. (2000) demonstrated that a thin marine cloud ($N = 50$ cm^{-3}) or a thick polluted one ($N = 150$ cm^{-3}) with very distinct DSDs could have the same r_{eff}. Obviously such different clouds, despite having similar r_{eff}, have different SSPs. Neglecting the influence of the DSD shape when parameterizing SSPs in terms of r_{eff} thus results in a second source of uncertainty when computing bulk radiative properties, hereafter called *SSP-uncertainty*. This highlights that the DSD shape assumption is critical both for r_{eff} estimation and for the subsequent SSPs estimation in terms of r_{eff}. To remain consistent, the same assumption should be made for both steps. This will be carefully ensured in this study.

In practice, one objective of this study is to derive a set of cloud optical properties parameterizations in the following form:

$$Q_{\text{ext}}^i, \omega^i, g^i = f^i(\text{LWC}, N, \text{DSD shape}, \text{Spectral averaging method}), \tag{6}$$

where i refers to individual spectral bands and DSD shape corresponds to a set of lognormal and modified gamma distributions. By implementing these new parameterizations in ecRad, this paper aims at quantifying the contribution of each uncertainty component on the estimation of CRE.
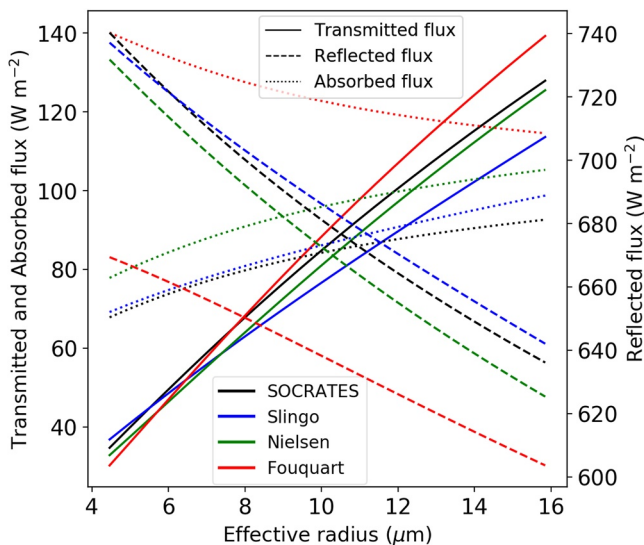
2.2. Preliminary Sensitivity Study

Before implementing the new parameterizations and to give a first hint of the impact of the choice of SSPs on cloud bulk radiative properties, preliminary radiative transfer simulations are performed on an ideal 1D cloud (having a vertically homogeneous LWC of 0.6 g m^{-3}, see details in Section 4.1) with the radiative code ecRad (presented in more details in Section 3.4). In ecRad, two options are natively available to compute the SSPs from r_{eff}, namely *Slingo* (Slingo & Schrecker, 1982) and *SOCRATES* (Edwards & Slingo, 1996; Manners, 2015). Both parameterizations are based on DSD observations dating back to the 70s (Hansen, 1971; Stephens, 1978). In addition, the parameterizations of Nielsen et al. (2014), which was derived from rigorous Lorenz-Mie calculations, and that of Fouquart (1988), which uses also Mie calculations applied to a stratus cloud (described in Hansen, 1971), were implemented. These parameterizations are then used to simulate transmitted (at cloud base) and reflected (at cloud top) fluxes, as well as atmospheric absorption (in-cloud), as a function of r_{eff} (Figure 2). The optical thickness of the cloud is about 126 (at the reference wavelength of 0.55 μm) for $r_{\text{eff}} = 10$ μm. Note that this experiment is limited to the r_{eff} range of 4–16 μm, since the Slingo parameterization is not valid out of this range. The resulting differences can reach several tens of W m^{-2} for fluxes. The lower transmittance obtained with the Slingo parameterization compared to the Nielsen parameterization is in agreement with the

Figure 2. Transmitted, reflected and absorbed fluxes computed for an ideal cloud (details in Section 4.1) with the *Slingo*, *SOCRATES*, *Nielsen* and *Fouquart* SSPs parameterizations, as a function of r_{eff}.
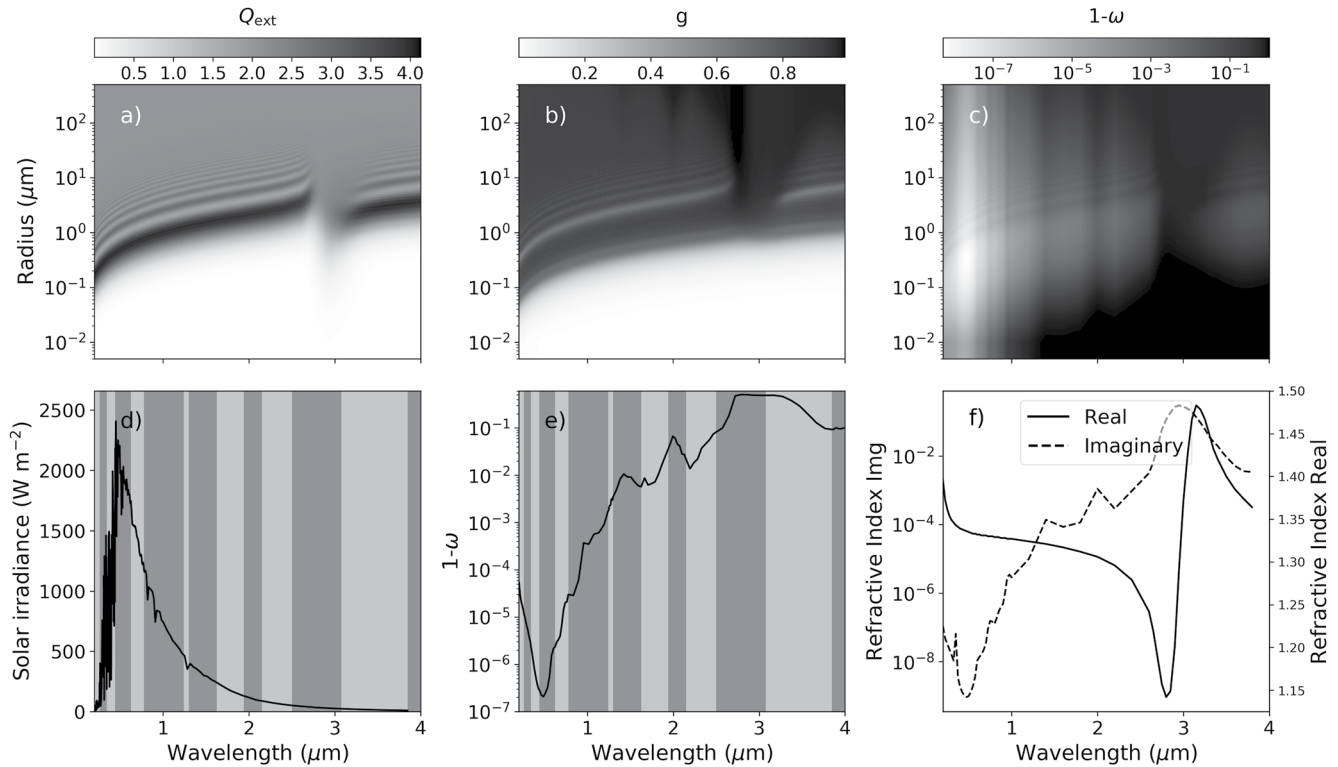
Figure 3. Maps of (a) extinction efficiency (b) asymmetry parameter and (c) co-albedo as a function of radius and wavelength. (d) Solar spectrum from Kurucz (1994). (e) Spectral variations of 1-ω for $r = 10\,\mu m$. Background shades in (d and e) correspond to ecRad spectral bands. (f) Imaginary and real parts of water refractive index (Hale & Querry, 1973).

findings of Nielsen et al. (2014). Differences are hard to trace back to physical reasons because the way those parameterizations were developed (in particular regarding the reference DSDs that were used) is not sufficiently detailed in the reference papers. Nevertheless this highlights the importance of cloud SSPs parameterization and the need to assess in a transparent and consistent way its impact on simulated cloud radiative properties.

3. Methodology

This section details how the new parameterizations of cloud SSPs are derived, accounting for DSD shape and spectral averaging. In the end these parameterizations take the form of simple analytical formulas in terms of r_{eff} to facilitate their implementation in any radiative transfer code.

3.1. Computation of Average SSPs Over Droplet Size Distribution and Spectral Bands

Here we consider that r_{eff} has been estimated from LWC and N assuming a particular DSD. The following aims at expressing the SSPs in terms of r_{eff}, assuming the same DSD. The first step thus consists in reconstructing the full DSD based on r_{eff} and the shape parameter (σ or ν). This is straightforward, because r_n can be expressed in terms of r_{eff} and the shape parameter (see Table 1). SSPs for individual droplet radius r and incident wavelength λ have been tabulated from Lorenz-Mie computations (using the Python module *pymiecoated*, based on Mätzler [2002], and the refractive index of liquid water from Hale and Querry [1973]). Figures 3a–3c show the variations of SSPs as a function of r and λ. A characteristic feature is the marked oscillations with r when r is close to the wavelength of the incident light. Figure 3f also highlights that the spectral variations are closely related to the spectral variations of the liquid water refractive index. For a given wavelength the SSPs are first integrated over the DSD as follows:

$$Q_{\text{ext}}(\bar{r}, \lambda) = \frac{\int Q_{\text{ext}}(r, \lambda) r^2 p(r) \mathrm{d}r}{\int r^2 p(r) \mathrm{d}r}, \tag{7}$$

$$g(\bar{r}, \lambda) = \frac{\int g(r)Q_{\text{sca}}(r, \lambda)r^2 p(r)\mathrm{d}r}{\int Q_{\text{sca}}(r, \lambda)r^2 p(r)\mathrm{d}r}, \tag{8}$$

$$\omega(\bar{r}, \lambda) = \frac{\int Q_{\text{sca}}(r, \lambda)r^2 p(r)\mathrm{d}r}{\int Q_{\text{ext}}(r, \lambda)r^2 p(r)\mathrm{d}r}, \tag{9}$$

where $\bar{r}$ denotes the average over the DSD and Q_{sca} corresponds to the fraction of the geometrical cross sectional area that contributes to the scattering of light. The integration is performed numerically by computing the SSPs on the interval 0.01–500 μm, splitted into 10,000 logarithmically spaced sub-intervals. This ensures that the oscillations pointed out in Figure 3 are properly captured. This configuration has been validated against the widely used code of Mishchenko et al. (1999).

The SSPs are then averaged over the spectral bands of the radiative code. This can be done as in Equation 11 of Slingo and Schrecker (1982), weighting the SSPs by the incident solar radiation at the top of atmosphere $S(\lambda)$ (Kurucz, 1994) shown in Figure 3d:

$$Q_{\text{ext}}(\bar{r}, \bar{\lambda}) = \frac{\int Q_{\text{ext}}(\bar{r}, \lambda)S(\lambda)\mathrm{d}\lambda}{\int S(\lambda)\mathrm{d}\lambda}, \tag{10}$$

$$g(\bar{r}, \bar{\lambda}) = \frac{\int g(\bar{r}, \lambda)Q_{\text{ext}}(\bar{r}, \lambda)\omega(\bar{r}, \lambda)S(\lambda)\mathrm{d}\lambda}{\int Q_{\text{ext}}(\bar{r}, \lambda)\omega(\bar{r}, \lambda)S(\lambda)\mathrm{d}\lambda}, \tag{11}$$

$$\omega(\bar{r}, \bar{\lambda}) = \frac{\int \omega(\bar{r}, \lambda)Q_{\text{ext}}(\bar{r}, \lambda)S(\lambda)\mathrm{d}\lambda}{\int Q_{\text{ext}}(\bar{r}, \lambda)S(\lambda)\mathrm{d}\lambda}, \tag{12}$$

where $\bar{\lambda}$ indicates the average on the spectral band. The linear averages displayed in Equations 10–12 are hereafter named *thin averaging*, after Edwards and Slingo (1996). Note, however, that alternatives for the spectral averaging are introduced in the next section. For the spectral integral, 280 wavelengths are used, which corresponds to 20 linearly distributed wavelengths for each of the 14 spectral bands of ecRad (these bands are depicted in Figures 3d and 3e).

The reference SSPs have been computed for 8 different DSD shapes, namely $\sigma = \{0.2, 0.35, 0.65, 0.9\}$ for the lognormal and $\nu = \{1, 5, 15, 30\}$ for the modified gamma. These ranges are consistent with the extreme values reported in Miles et al. (2000). For each shape the SSPs have been computed for 80 values of r_{eff} ranging from 1 to 50 μm.

3.2. Spectral Averaging Methods

The co-albedo 1-ω features large variations across the SW, and within individual bands of ecRad. Figure 3e, which shows the spectral variations of 1-ω for $r = 10$ μm, demonstrates that 1-ω can vary by up to 3 orders of magnitude across a single spectral band. Since the bulk optical properties of scattering media are highly non-linear in terms of the SSPs, which is a consequence of multiple scattering, using linear spectral averaging as in Equations 10–12 may bias the estimated cloud radiative properties. This was already pointed out by Edwards and Slingo (1996), and is further explained below.

Neglecting the effect of gases, the reflectance and transmittance of a homogeneous cloud can be computed using the two-stream approximation (see Appendix A). They can be formally written as (expanded in Equations A1 and A2):

$$T = T_{2S}(\omega, g, \tau), \tag{13}$$

$$R = R_{2S}(\omega, g, \tau), \tag{14}$$

where $2S$ stands for two-stream and τ is the optical thickness of the cloud of geometrical thickness H. By definition (Stephens, 1978; Xu et al., 1996):
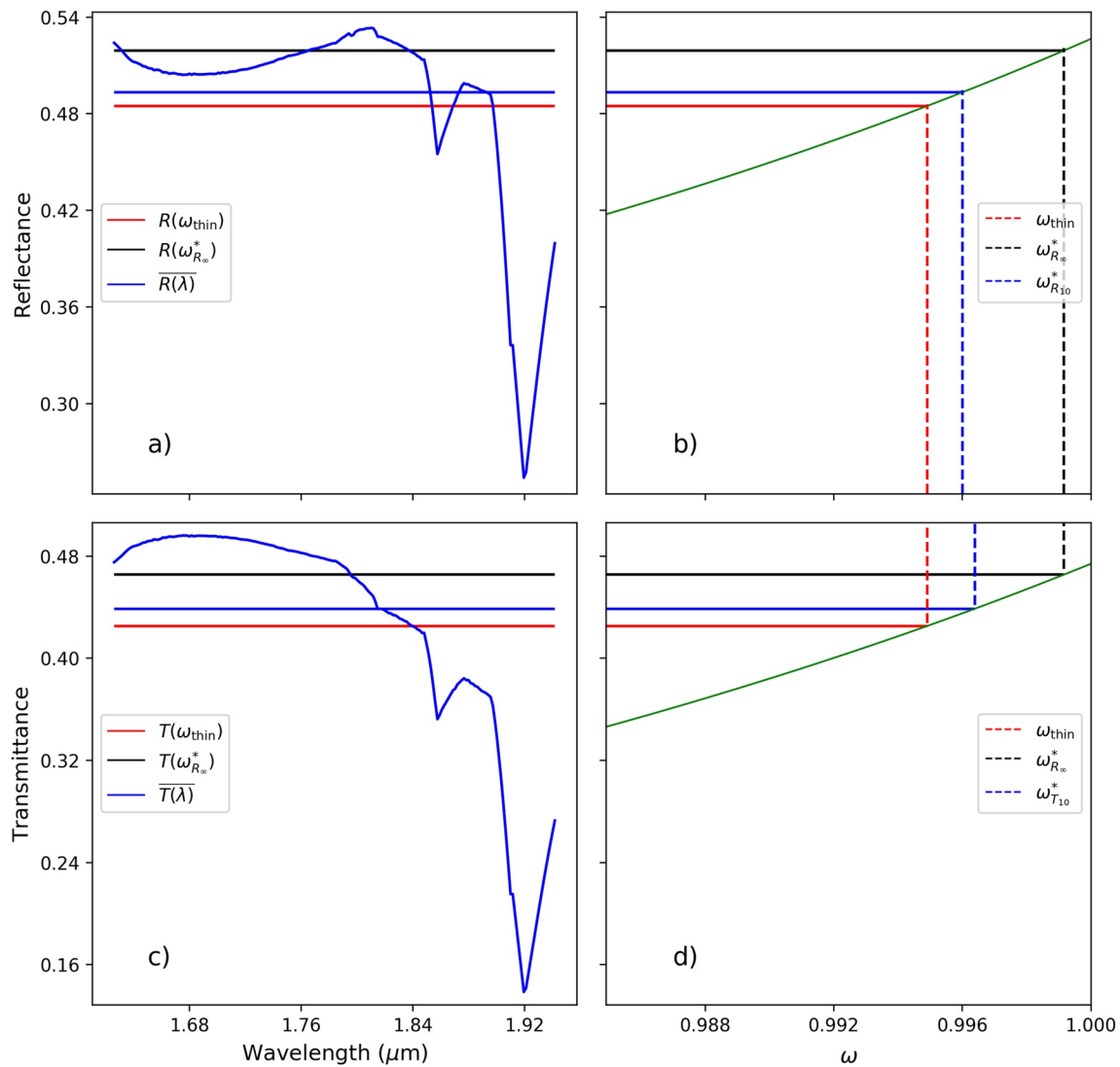
Figure 4. The blue curves in (a and c) show the reference reflectance and transmittance for the spectral band 1.62–1.94 μm, computed with Equations 13 and 14. The horizontal blue lines show the average of these quantities over the spectral band, weighted by the TOA solar spectrum. In (b and d) the green curves show the relation between the monochromatic reflectance, transmittance and ω computed from Equations A1 and A2, using thin averaged values for $\bar{g}$ and $\bar{Q}_{ext}$. The red lines indicate the results of Equations 13 and 14 applied to the thin average ω (ω_{thin} highlighted by the blue dashed lines) while the black lines indicate the results of Equations 13 and 14 applied to the thick average ω ($\omega_{R_\infty}^*$ highlighted by the black dashed lines). All the computations were made for a cloud with $\tau = 10$ (at $\lambda = 0.55$ μm), $r_{eff} = 10$ μm and $\sigma = 0.2$. The dashed blue lines highlight the value that ω should take over that spectral band to match the reflectance ($\omega_{R_{10}}^*$) or transmittance ($\omega_{T_{10}}^*$). Note that $\omega_{R_{10}}^* \neq \omega_{T_{10}}^*$.

$$\tau(\lambda) = H \int Q_{ext}(r, \lambda)\pi r^2 n(r)\, \mathrm{d}r \tag{15}$$

$$= \frac{3Q_{ext}(\bar{r}, \lambda)\mathrm{LWP}}{4r_{eff}\rho_w}, \tag{16}$$

where LWP is the liquid water path of the layer, defined as:

$$\mathrm{LWP} = H\ \mathrm{LWC}. \tag{17}$$

Using Equations 13 and 14, $T(\lambda)$ and $R(\lambda)$ of an ideal cloud layer with $r_{eff} = 10$ μm and $\tau = 10$ (at $\lambda = 0.55$ μm) are computed at high spectral resolution in the band 1.62–1.94 μm, and depicted by the blue curves in Figure 4. The horizontal blue lines show the corresponding averages over the band (weighted by $S(\lambda)$), hereafter named

true properties. We define ω^*, the band-averaged value ω should take for this band to ensure that the transmittance (reflectance) computed from band-averaged properties with Equation 13 (14) equals the true transmittance (reflectance). These are depicted by the dashed blue lines projections in Figures 4b and 4d, where the green lines correspond to Equations 13 and 14 with g and τ corresponding to thin averages. The value ω_{thin} corresponding to thin averaging is highlighted by the red line. Once projected on the left panels it results in about 2% relative errors in reflectance and transmittance compared to the true values. This highlights that using thin averaging to estimate band-averaged $\bar{\omega}$ is not accurate. This is the result of absorption saturation within the band. The linear average $1-\bar{\omega}$ underestimates (resp. overestimates) absorption in the wavelengths where highly absorbing (resp. less absorbing) features of liquid water are present. Depending on the solar energy available in that band this can lead to broadband overestimation or underestimation of absorption.

To circumvent this issue, Edwards and Slingo (1996) have introduced the notion of *thick averaging*. Starting from the statement that $\overline{Q_{\text{ext}}}$ and $\bar{g}$ slightly vary across the SW, they used thin averaging (Equations 10 and 11) to compute the band-averaged quantities for these variables. To approximate ω^* they used a formula equivalent to Equation 14, assuming in addition that $\tau = \infty$, implying that any cloud can be considered optically thick. In this case $\omega^*_{R_\infty}$ can be estimated from $\bar{g}$ and $\overline{R_\infty(\lambda)}$. Although many clouds are indeed optically thick, many are not. For instance, the black lines in Figure 4 show that T and R estimated using $\omega^*_{R_\infty}$ are as inaccurate as using thin averaging for this particular cloud. In addition, this approach allows to match the reflectance of optically thick clouds, but not their transmittance, a quantity that is also of interest in our study. In order to generalize this strategy to transmittance and to any optical thickness, various expressions for ω^* are derived, based on the inversion of Equations A2 or A1 for various optical thicknesses ($\tau = 1$, 10 and 20). These 6 new methods are noted T_1, T_{10}, T_{20} and R_1, R_{10}, R_{20}. These parameterizations can be formally written as:

$$\omega^*_{X_\tau} = \omega \quad \text{such that} \quad X(\omega, \bar{g}, \bar{\tau}) = \overline{X(\omega(\lambda), g(\lambda), \tau(\lambda))}, \tag{18}$$

where X can be either R or T, and $\overline{}$ indicates thin averaging. It is worth noting that Ritter and Geleyn (1992) have suggested an approach somehow similar to the transmittance-based methods (T_1, T_{10}, T_{20}). They searched an ω which would provide accurate fluxes below clouds of various optical thicknesses. However in their computations, multiple scattering was ignored. Fouquart and Bonnel (1980) also derived an empirical equation which relates $1-\omega$ to the total optical thickness of the cloud, in order to account for absorption saturation. However this sensitivity to total cloud optical thickness precludes using their parameterization within the individual layers of a cloud.

Figure 5a shows the broadband differences between the various spectral averaging methods and the reference two-stream computation for reflectance and transmittance, for clouds of various optical thicknesses. For instance, the error is 0 when the transmittance of a cloud of optical thickness 10 is computed with the parameterization T_{10}. This figure also confirms that reflectance and transmittance cannot be matched at the same time, which means that systematic errors are obtained when computing surface and TOA budgets using radiative codes with limited spectral resolution. Importantly, using thick averaging can result in significant errors even for large optical thicknesses. To clarify this, we have extended the optical thickness range and distinguished the errors related to reflectance and transmittance in Figures 5b and 5c. It can be noticed that thick averaging works well only for optical thicknesses higher than 200–300. This corresponds to extremely thick clouds, probably not representative of the majority of clouds on Earth.

To be exhaustive, the logarithmic average, used by Chou et al. (1998), was also included in the spectral averaging methods. In this case, $\overline{\omega}_{\text{log}}$ is computed as:

$$\overline{\omega}_{\text{log}} = 1 - \exp\left(\frac{\int \log(1 - \omega(\lambda)) Q_{\text{ext}}(\lambda) S(\lambda) \mathrm{d}\lambda}{\int Q_{\text{ext}}(\lambda) S(\lambda) \mathrm{d}\lambda} \right). \tag{19}$$

The 9 above mentioned spectral averaging methods (thin, thick, logarithmic, and the 6 new methods) are applied to all the considered DSD shapes to complete the whole set of parameterizations described by Equation 6. The obtained set of ω^* parameterizations allows to estimate the impact of spectral averaging on the overall uncertainty. It is worth noting that here the spectral averages are all weighted by the incident radiation at TOA, to remain consistent with the work of Edwards and Slingo (1996) and Slingo and Schrecker (1982), and to generalize the thick averaging approach. In addition gaseous absorption was not considered in the computation of ω^*. This might not be the most accurate strategy because the solar spectrum at cloud top can differ from that at TOA as a result of
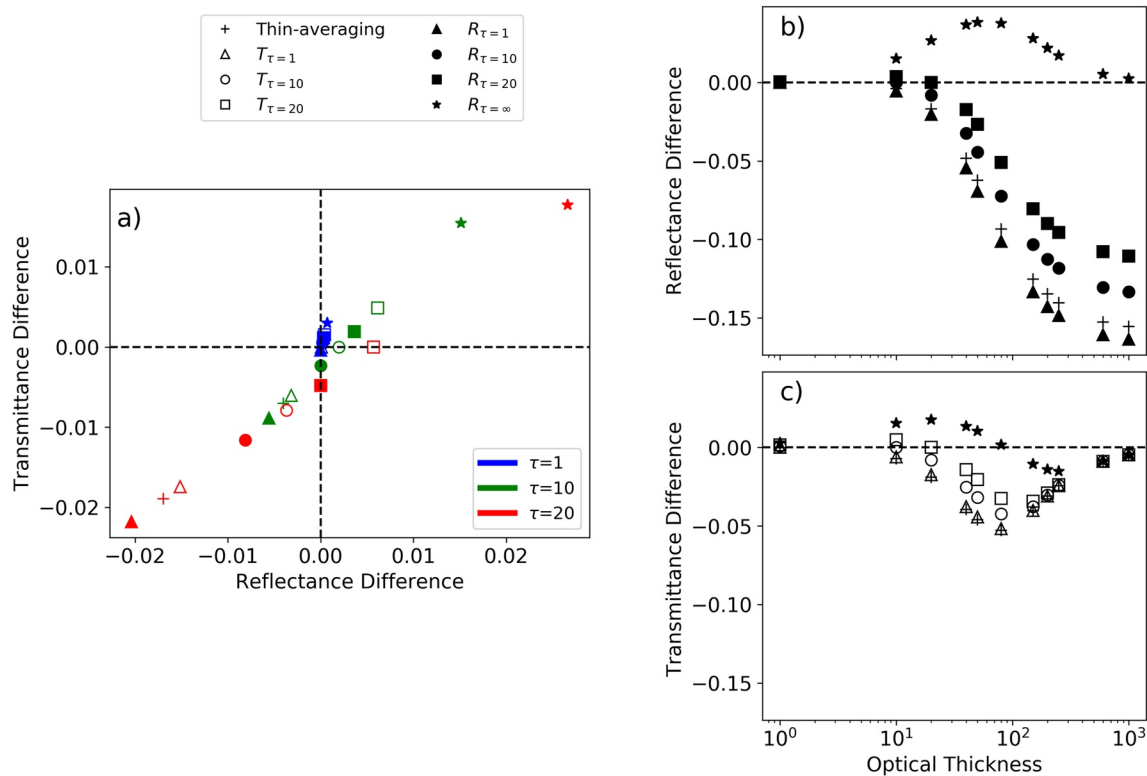
Figure 5. Differences in broadband SW (0.2–4 μm) transmittance and reflectance between the reference two-stream values and the quantities computed with various spectral averages of ω. These are calculated for a droplet size distribution with $r_{eff} = 10$ μm and $\sigma = 0.2$.

atmospheric absorption above the cloud. Also, as water vapor and cloud absorption are correlated, the averages may be biased due to an overestimation of radiation in water vapor absorption bands.

To resolve this issue, several strategies were proposed in the literature. Lu et al. (2011) used a correlated k-distribution approach consistent with what is done for the gases to derive cloud absorption. They demonstrated that their method can moderate the 30% error on heating rates obtained with the thin averaged 1-ω, relative to line-by-line calculations. However the contribution of considering the correlation between water vapor and droplet scattering, compared to that of the higher spectral resolution, is not quantified. In addition, they have used the average spectrum at 500 hPa to derive the average 1-ω. Although Dobbie et al. (1999) showed that using the typical spectrum at 500 hPa in Equations 10–12 did not change their calculations of the band mean SSPs, this could still contribute to the differences. The parameterization of Fouquart and Bonnel (1980) includes the contribution of a constant amount of water vapor in the cloud, since their parameterization was derived for a stratus cloud in the presence of an atmosphere. Räisänen (1999) proposed an exhaustive method to derive $1 - \bar{\omega}$ that not only accounts for the absorption of water vapor above the cloud, but also considers if other clouds are present above the evaluated cloud. Such strategies have not been replicated in this study because the focus is more on the uncertainties than on the absolute values. The correlation between water vapor and clouds remains a critical issue to derive the most accurate parameterizations, though.

3.3. SSPs Parameterizations in Terms of r_{eff}

Natively available SSPs parameterizations in ecRad consist of analytical expressions of SSPs in terms of r_{eff}. In order to implement the new parameterizations in ecRad, we mimic the analytical function used for the *SOCRATES* parameterization, which is based on Padé approximants (Manners, 2015). This allows straightforward inclusion of the new parameterizations in ecRad library, with minor changes to the core of the code. Once the SSPs have been computed for 80 individual r_{eff} in the range 1–50 μm for eight DSD shapes and nine spectral methods, they are fitted with the following functions:
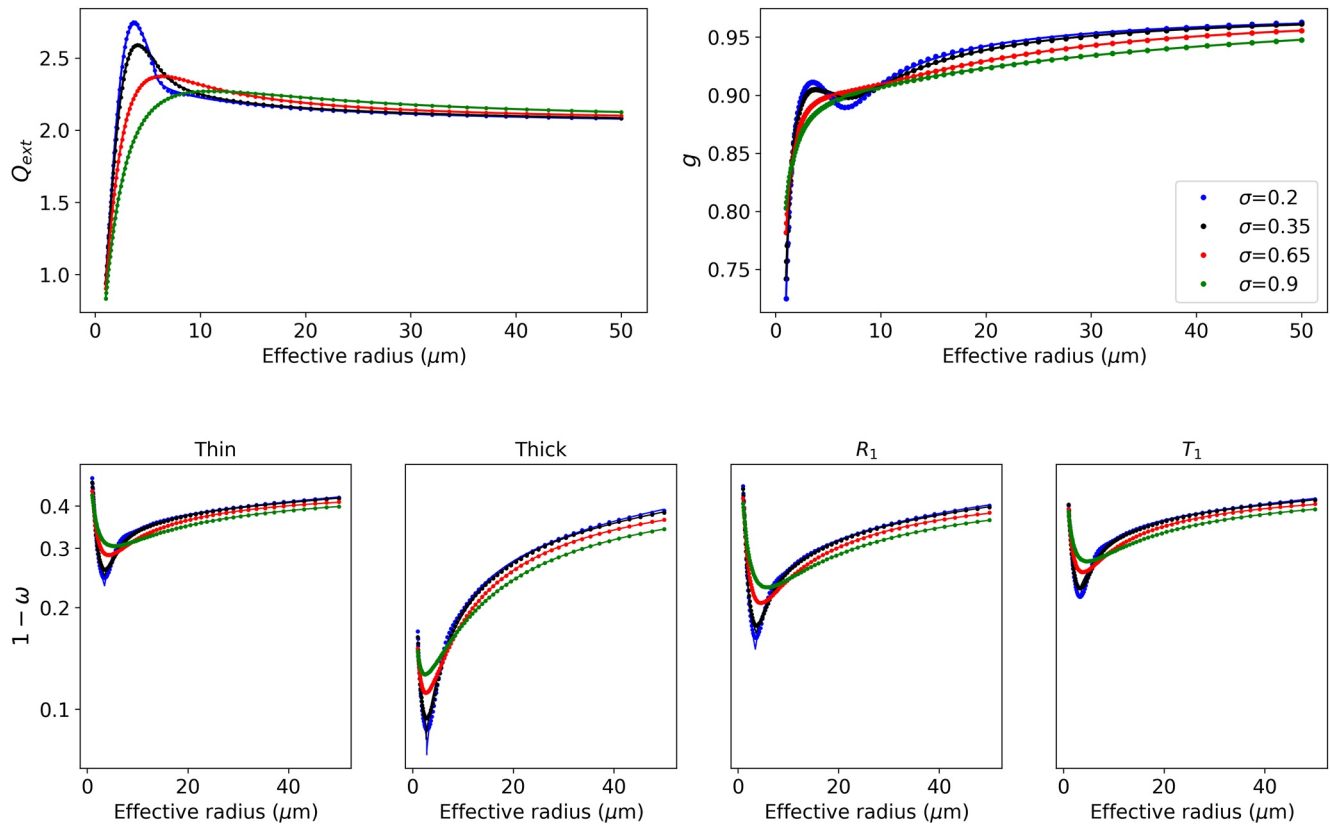
Figure 6. Single scattering properties of the 2.15–2.5 μm band in terms of r_{eff}, computed for various droplet size distributions (DSDs). The dots are the reference single scattering properties obtained from Lorenz-Mie calculations and the lines correspond to the fitted analytical functions. The colors depict four distinct lognormal DSDs. Each column in the lower row shows the single scattering albedo calculated with a different spectral method.

$$Q_{\text{ext}} = \frac{4}{3}\left(\frac{P_1 r_{\text{eff}} + P_2 r_{\text{eff}}^2 + P_3 r_{\text{eff}}^3}{1 + P_4 r_{\text{eff}} + P_5 r_{\text{eff}}^2 + P_6 r_{\text{eff}}^3}\right), \tag{20}$$

$$\ln(1 - \omega) = \ln\left(\frac{P_7 + P_8 r_{\text{eff}} + P_9 r_{\text{eff}}^2}{1 + P_{10} r_{\text{eff}} + P_{11} r_{\text{eff}}^2}\right), \tag{21}$$

$$g = \frac{P_{12} + P_{13} r_{\text{eff}} + P_{14} r_{\text{eff}}^2}{1 + P_{15} r_{\text{eff}} + P_{16} r_{\text{eff}}^2}. \tag{22}$$

The main difference with *SOCRATES* parameterization is the fact that two distinct fits are applied (the reference SSPs calculated with the Lorenz-Mie theory are shown with the dots in Figure 6) while ensuring continuity at the junction. This follows the strategy of Hu and Stamnes (1993) who separated their fits in three size ranges. This means that a total of 32 parameters are needed to describe the variations of SSPs with r_{eff}. This strategy ensures that the oscillations for small r_{eff} are well captured (see Figure 6), which would not be possible with a single term. It also prevents the function to diverge at small r_{eff}, as occurs for *SOCRATES*. Hence for each new parameterization a cut-point is provided that splits the fits into two. This cut-point was derived empirically for each spectral band. For Q_{ext} and g, the cut-point is set such that $r_{\text{eff}}/\lambda_{\text{center}} = 2$ (where λ_{center} denotes the central wavelength of the spectral band), which is approximately where the oscillations take place. However the latter constant does not work as well for 1-ω. Thus the local minima of the $1 - \omega$ curves (Figure 6 lower row) were selected as cut-points. Figure 6 shows an example of these two-part fits on the 2.15–2.5 μm band. It highlights that the strongest sensitivity to DSD is obtained for effective radii smaller than 10 μm. The differences can reach 50% for 1-ω and 25% for Q_{ext}. Finally, the obtained coefficients are introduced in ecRad in the form of a new netCDF file containing 33 values per spectral band (32 fit parameters and the cut-point value).

3.4. Configuration of ecRad

ecRad is a modular radiative scheme for SW and LW radiative fluxes computations, dedicated to atmospheric models. It was developed for the Integrated Forecasting System, the weather forecast model used operationally by the European Centre for Medium Range Weather Forecasts (ECMWF). In this paper its offline version is used (freely available for research use at https://github.com/ecmwf/ecrad/tree/master/ifs). The main inputs of this radiative code are the atmospheric profile (including aerosols and trace gas concentrations), the surface albedo and temperature, the solar zenith angle and TOA incident broadband irradiance. Note that in this study the simulations were performed without aerosols. The ozone profile in the ideal case corresponds to that of the I3RC experiment (detailed in Section 4.1) while for the real cases it comes from the US67 standard atmosphere. In the SW region, ecRad deals with 14 spectral bands, corresponding to those of RRTM (Mlawer et al., 1997; Morcrette et al., 2008). The new cloud SSPs have been computed on the same bands with the previously detailed parameterizations and were added to ecRad library. ecRad offers several options to solve the radiative transfer equation. In the present study, the McICA solver (Pincus et al., 2003) is used. The surface albedo is set to 0.2 and the fractional subgrid standard deviation of LWP is set to 0.75 (Ahlgrimm et al., 2018). The simulations are performed for a solar zenith angle of 40°. The downwelling solar irradiance at the top of atmosphere is set to 1366 W m^{-2}.

4. Results

The newly developed parameterizations are now used to investigate how limited knowledge of the DSD shape impacts the estimation of CRE. The parameterizations are thus applied to various 1D cloudy profiles and the focus is on the energy transmitted below the cloud, reflected at the top of the cloud, and absorbed within the cloud. The profiles comprise an ideal profile based on the I3RC reference profile (Cahalan et al., 2005), and more realistic cases derived from horizontally averaged 3D fields of large eddy simulations (LES) performed with the Meso-NH research model (Lac et al., 2018). Finally ecRad was applied to outputs of the climate model CNRM-CM6-1 (Roehrig et al., 2020; Voldoire et al., 2019) to compute CRE. The DSD shape impact is assessed for all cases both in terms of *SSP-uncertainty* and r_{eff}-*uncertainty*.

4.1. Ideal Case

The goal of this ideal case is to explore a variety of LWC in order to assess the impact of the DSD assumption on simulated cloud bulk radiative properties. The input profile is based on the I3RC cloud, which extends between 1,000 and 2,400 m. The total number concentration of cloud droplets is set to 200 cm^{-3}. r_{eff} is computed from Equation 5. The simulations are carried out with all the new parameterizations, ensuring that the value of k in Equation 5 is consistent with the DSD shape of the SSPs parameterization. The fluxes reflected at the top of the cloud, transmitted through the cloud layer, and absorbed in cloud, are computed with ecRad. The simulations were performed for 100 values of LWC in the range 0.02–1 g m^{-3}, which corresponds to LWP ranging from 0.028 to 1.4 kg m^{-2}. The results of these experiments are shown in Figure 7.

For nearly all bulk radiative properties the envelope of the lognormal parameterizations is wider than that of the modified gamma. The spread for transmitted energy at cloud base, reflected energy at cloud top and absorbed energy in the lognormal case rises up to 141, 147 and 14 W m^{-2} respectively (these maximal differences correspond to the lowest values of LWC for reflectance and transmittance and to the highest value of LWC in the absorptance case) while the counterpart values for the modified gamma are 91, 96 and 10 W m^{-2}. In the following, the uncertainties will be assessed using only the lognormal DSDs with $\sigma = 0.2$ and $\sigma = 0.65$, which roughly corresponds to the 5th and 95th percentiles of the values reported by Miles et al. (2000). To quantify the impact of spectral averaging, simulations were run with a lognormal DSD ($\sigma = 0.2$), with all available spectral averaging methods. Figure 8 shows the radiative properties calculated with 6 methods (T_1, R_1, R_{10}, T_{10}, thick averaging R_∞ and logarithmic), in terms of the differences with respect to thin averaging.

The range observed in absorbed energy (8 Wm^{-2}) is more significant than that of reflectance and transmittance (6 and 2.5 Wm^{-2}, respectively). This is expected because the spectral averaging method mostly affects cloud absorption via 1-ω, but not cloud optical thickness which is the main driver of cloud transmittance and reflectance. This is in agreement with the results of Edwards and Slingo (1996). For their 24 band model, which is similar to ecRad spectral resolution, they reported differences of 8 and 6 W m^{-2} in absorbed energy for an optically thin ($\tau = 10$) and thick ($\tau = 100$) cloud, respectively, between the thin and thick averaging methods.
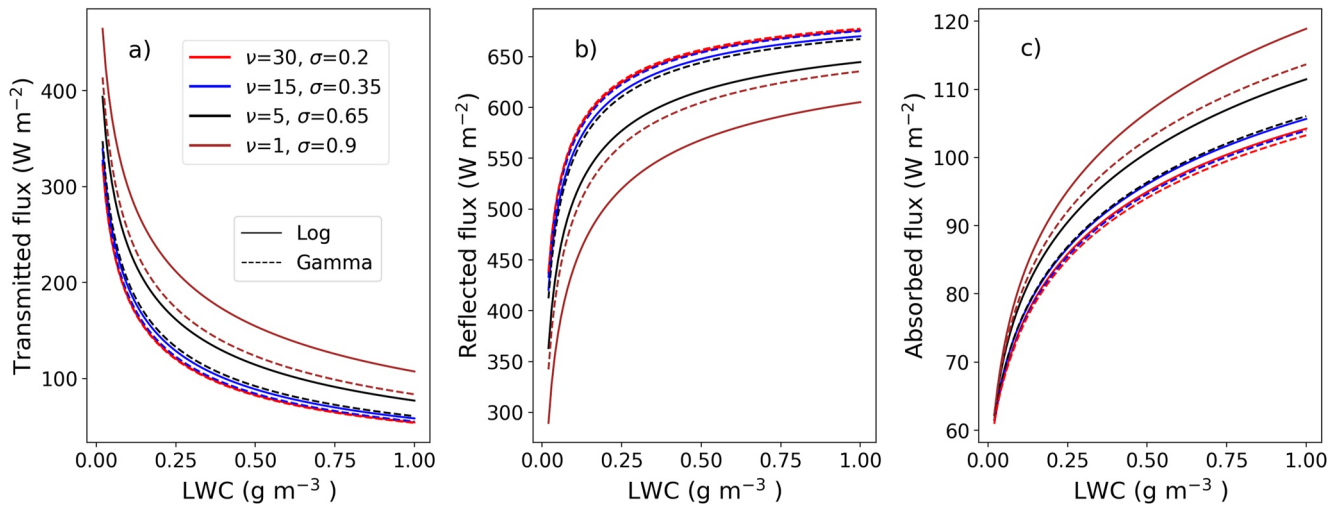
Figure 7. Bulk radiative properties of the ideal cloud as a function of liquid water content (LWC), computed for lognormal (full lines) and modified gamma (dashed-line) distributions using thin spectral averaging. As the cloud geometrical thickness is fixed, increasing the LWC implies increasing the LWP.

T_1 and R_1 methods are close to thin averaging results and become closer as LWC increases. Another noticeable trend is that the thick averaging and logarithmic methods significantly diverge from thin averaging, as LWC—and consequently cloud optical thickness—increases. Conversely, for the lower optical thicknesses all spectral methods are relatively close. This is because differences in absorption and scattering are not enhanced by multiple scattering in thin clouds.

In Figure 7 the same DSD shapes were used for r_{eff} diagnostic and SSP parameterization. However, each of these two steps generate their own uncertainty. In order to quantify the contribution of each step to the overall uncertainty, two additional simulations were performed:

1. Two DSDs with $\sigma = 0.2$ and $\sigma = 0.65$ are used for the SSP parameterization while r_{eff} is estimated using the k value of 0.67, which corresponds to the recommendation of Martin et al. (1994) for continental clouds and is close to the value corresponding to $\sigma = 0.35$ (Figure 1).
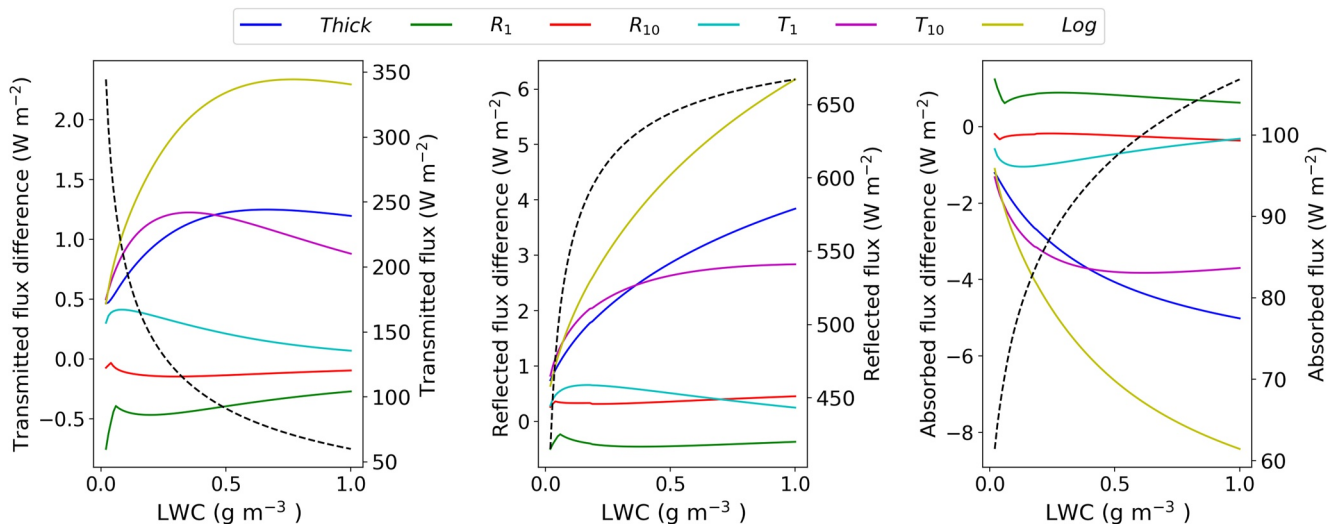

Figure 8. Differences (with respect to thin averaging) in bulk radiative properties of the ideal cloud as a function of liquid water content, for various spectral averaging methods (thick, logarithmic, R_1, R_{10}, T_1 and T_{10}), calculated only for lognormal droplet size distribution of $\sigma = 0.2$. The dashed black lines show the bulk radiative properties calculated using the thin averaging method (right y-axis).
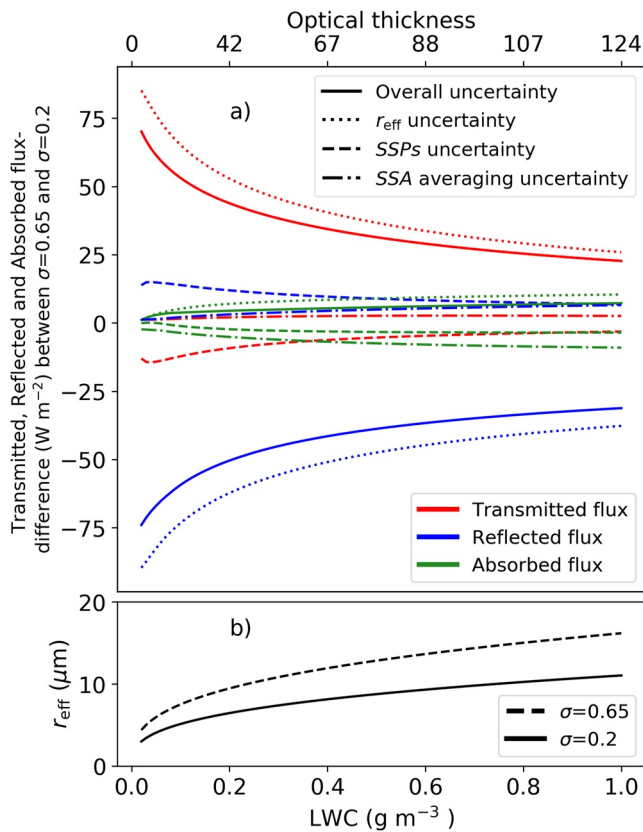
Figure 9. (a) Overall droplet size distribution-related bulk radiative properties uncertainty (solid lines), r_{eff}-uncertainty (dotted lines), *SSP-uncertainty* (dashed lines) as a function of liquid water content (g m^{-3}), all being calculated with the thin averaging method. The uncertainties related to the spectral averaging method are shown with dashed-dotted lines, for $\sigma = 0.2$. Red, blue and green colors depict the uncertainties in transmitted, reflected and absorbed flux, respectively. The upper *x*-axis shows the equivalence of lower axis in terms of optical thickness calculated using Equations 5 and 16, with $k = 0.67$. (b) Variations of r_{eff} with LWC for $\sigma = 0.2$ and $\sigma = 0.65$.

2. r_{eff} is estimated assuming distinct k values corresponding to the above mentioned σ, but the SSP parameterization is the same, corresponding to $\sigma = 0.35$.

These configurations are used to simulate the bulk radiative properties of the ideal cloud, using only thin averaging. The differences between bulk radiative properties obtained in all configurations are shown in Figure 9a. Dashed lines highlight the *SSP-uncertainty* and the dotted lines highlight the r_{eff}-uncertainty. The solid lines show the overall differences when the DSD shape is consistent throughout both steps. The overall differences in transmitted and reflected fluxes reach 70 and 74 W m^{-2}. The corresponding surface and top of the cloud fluxes equal 323 and 437 W m^{-2} for $\sigma = 0.2$. Figure 9 also shows that the r_{eff}-uncertainty dominates over the *SSP-uncertainty*. Interestingly, the *SSP-uncertainty* slightly offsets (by about 20%) the r_{eff}-uncertainty. Maximum uncertainties of 89, 85 and 10 W m^{-2} in reflected, transmitted and absorbed fluxes due to the r_{eff}-uncertainty are indeed compensated by 15, 14 and 3.5 W m^{-2} uncertainties due to the *SSP-uncertainty*. Looking at the effective radii corresponding to the investigated range of LWC in Figure 9b, it can be deduced that the r_{eff}-uncertainty results from a nearly 50% increase of the effective radius when σ changes from 0.2 to 0.65.

To highlight the effect of spectral averaging, the dash-dotted lines in Figure 9 show the differences between two extreme methods, namely the R_1 and logarithmic methods. In this case both steps relied on the lognormal DSD with $\sigma = 0.2$. It confirms that the absorption is more sensitive to the spectral averaging uncertainty than reflectance and transmittance.

Based on the above results, only two extreme spectral averaging methods are selected to estimate uncertainties in the next sections.

4.2. Real Cases

Four LES simulations were used to construct the realistic 1D profiles used in this section. They are presented, along with the methodology to convert 3D outputs into 1D profiles. Then the results of ecRad simulations are discussed. The profiles of LWC are shown in Figure 10.

4.2.1. Description of the Cases

The 4 reference cases have been simulated with the Meso-NH model. To extract 1D profiles of temperature, pressure, relative humidity and LWC from the 3D output fields, the quantities are averaged over the domain, including only cloudy columns (columns where at least one layer has a LWC larger than 10^{-6} kg kg^{-1}). The cloud fraction is then set to 1 for all cloudy grids. The value of N is fixed at 200 cm^{-3}. The following provides specific details for each simulation.

4.2.1.1. Fog

This is a simulation of a fog event observed at Cardington (UK) on the night of 24–25 November 2014 during the Local and Non-local Fog Experiment (LANFEX, Price et al., 2018). This is a typical case of radiative fog forming in a nocturnal stable boundary layer and developing over several hours into an optically thick fog. An intercomparison exercise was built on this case, involving LES and single column model simulations from different models. The vertical profile used in this study comes from a simulation using the 2-moment microphysical scheme LIMA (Vié et al., 2016) with a typical aerosol population for Cardington (3MOD experiment described in Ducongé, 2019). The transition to a thick fog occurs a bit too fast and the fog top height is overestimated compared to observations, but the vertical distributions of LWC and N are in good agreement with observations, with maximum values found near the top of the fog layer. Note that the N value computed by LIMA is not used in our 1D simulations. The optical thickness of the fog is about 3.
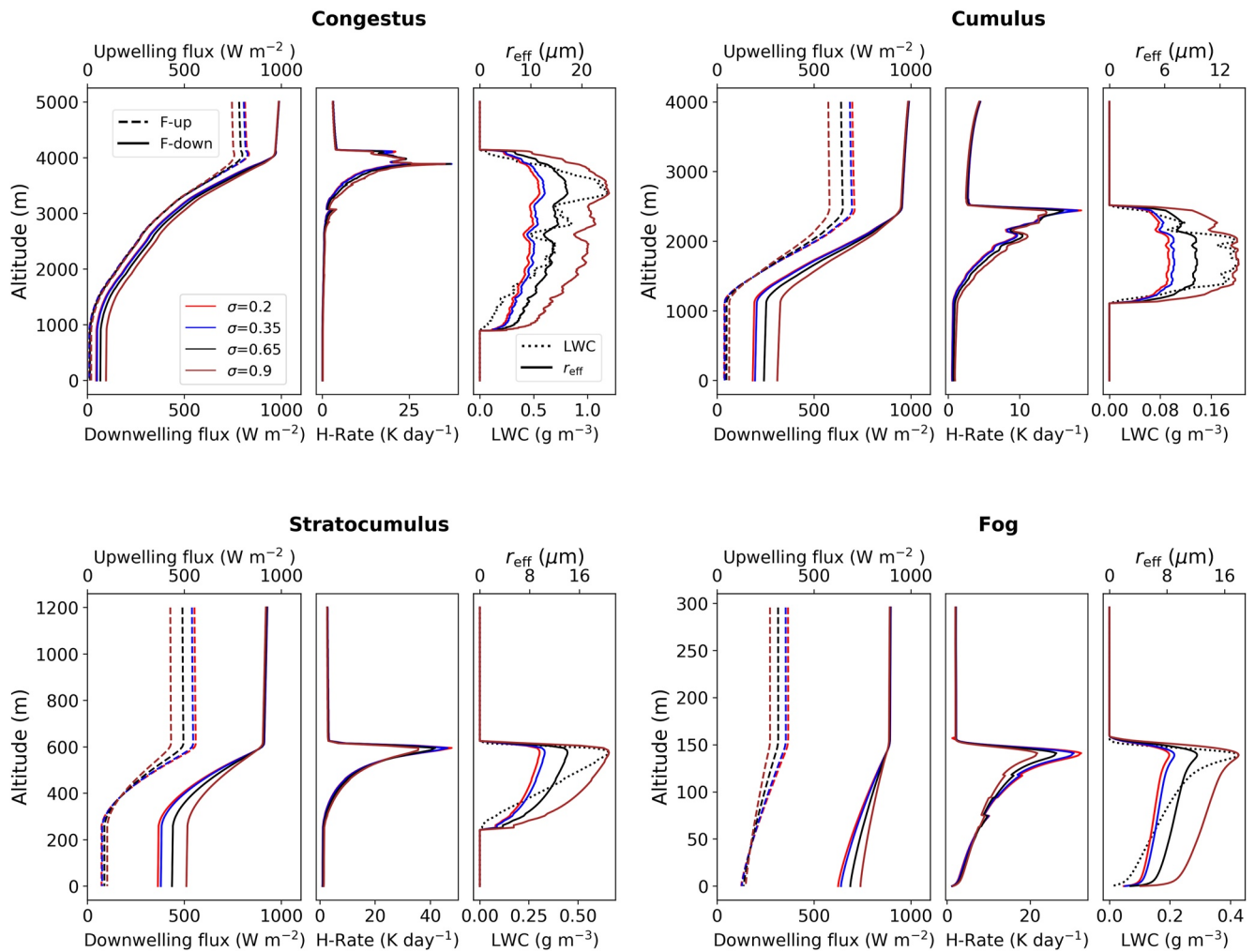
Figure 10. For each large eddy simulation (congestus, comulus, stratocumulus and fog), from left to right, shortwave radiative fluxes, heating rates and effective radii profiles, calculated for the lognormal droplet size distributions with $\sigma = \{0.2, 0.35, 0.65, 0.9\}$ (shown with different colors). The black dotted lines in the right panel shows the liquid water content profile.

4.2.1.2. Stratocumulus

This is a simulation of a stratocumulus based on the First International Satellite Cloud Climatology Project Regional Experiment model intercomparison study (Duynkerke et al., 2004), inspired from observations above the Pacific Ocean, off the coast of California, acquired in July 1987. The LES simulation used here is detailed in Brient et al. (2019) and the profiles provided to ecRad are extracted from the simulation during nighttime at a time of maximum vertical extension of the stratocumulus. The optical thickness of this cloud is about 8.

4.2.1.3. Cumulus

This is a simulation of continental shallow cumulus based on the ARMCU model intercomparison study (Brown et al., 2002) inspired from observations on 21 June 1997 at the Southern Great Plains site of the Atmospheric Radiation Measurement. This case corresponds to a diurnal cycle of shallow convection and the profiles provided to ecRad were extracted after 9 hr of simulation, the time of maximum development of the shallow clouds. The optical thickness of the cumulus is close to 20.

4.2.1.4. Congestus

This is a simulation of a congestus cloud in growing phase simulated at very high-resolution (5 m) (Strauss, 2020). This simulation was nested around a selected congestus cloud from a 50 m-resolution simulation of a population of clouds. The optical thickness of this congestus is around 100.
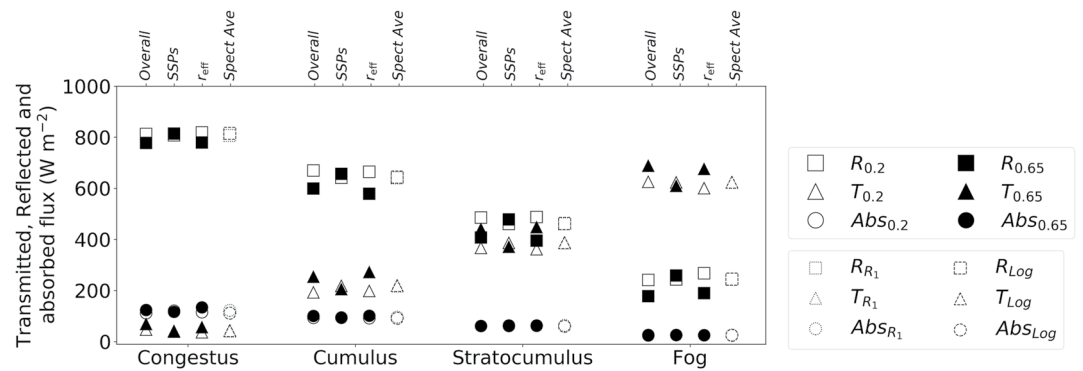
Figure 11. Bulk radiative properties of the 4 real cases calculated using two droplet size distribution shapes of $\sigma = 0.2$ and $\sigma = 0.65$. First column: consistently in both r_{eff} and single scattering properties (SSPs) parameterizations. Second column: only in SSPs parameterization (using r_{eff} computed with $\sigma = 0.35$), Third column: only in r_{eff} estimation (using the $\sigma = 0.35$ in SSPs parameterization). Fourth column: radiative properties obtained with the two extreme spectral averaging methods, with $\sigma = 0.2$.

4.2.2. Results of Simulations

ecRad was applied to the 1D profiles, completed above the simulation domain with the US67 standard atmospheric profile up to 80 km. The simulations were performed with the 4 lognormal DSD shapes, again restricting to thin averaging. Figure 10 depicts the upwelling (dashed lines) and downwelling (solid lines) fluxes, hereafter called $F_i^\uparrow$ and $F_i^\downarrow$, where i indicates the corresponding DSD shape (σ value). The cloud boundaries can be deduced from the LWC profiles shown in black dotted lines in the third panel of each case. Generally it can be seen that the cloud with DSD shape of $\sigma = 0.2$ is more opaque than that of $\sigma > 0.2$. This can be explained by looking at the effective radius profiles on the third panel (solid color lines). For example, for any cloudy layer in our model, the effective radius for a DSD with $\sigma = 0.65$ is about 50% larger than that of $\sigma = 0.2$. According to Equation 16 the optical thickness will be larger for $\sigma = 0.2$, resulting in larger reflectance and lower transmittance. This explains why $F_{0.2}^\downarrow$ at the surface ($F_{0.2}^\uparrow$ at the top) is smaller (greater) than $F_{0.65}^\downarrow$ ($F_{0.65}^\uparrow$). In addition to the fluxes, the heating rates are also displayed to highlight differences in atmospheric absorption. It suggests that changing the DSD shape from $\sigma = 0.2$ to $\sigma = 0.65$ can alter the heating rates from 1% in the cumulus case (higher optical thickness) up to 17% in the fog case (lower optical thickness).

As for the ideal case, we distinguish the contributions of r_{eff}-uncertainty and SSP-uncertainty. For each real case, switching between $\sigma = 0.2$ and $\sigma = 0.65$ produces distinct results in terms of bulk radiative properties, illustrated with filled and empty geometrical shapes in Figure 11. The difference between identical filled and empty shapes for each case demonstrates the overall DSD-related uncertainty in the first column, the SSP-uncertainty in second, and r_{eff}-uncertainty in the third column. The uncertainty due to the DSD shape can reach 80 W m^{-2} on transmitted/reflected fluxes for the fog and stratocumulus cases having LWP amounts of 0.028 and 0.12 kg m^{-2}, respectively. For the cumulus and congestus cases where the liquid water path reaches 0.19 and 1.8 kg m^{-2}, respectively, lower differences are obtained for transmitted and reflected fluxes. It must be noted that while cumulus and stratocumulus clouds have close values of LWP, they differ significantly in terms of bulk radiative properties. This is due to the lower values of LWC in cumulus, which results in a greater optical thickness (see Equations 5 and 16).

Similarly to the ideal case results, it is observed that SSP-uncertainty partly offsets the r_{eff}-uncertainty on reflected, transmitted and absorbed fluxes by 17%, 13% and 22% for the congestus case. Approximately similar results are obtained for the cumulus case. In the fog and stratocumulus cases the offset reaches 20% and 19% for reflected and transmitted fluxes. Regarding absorption, SSP-uncertainty amplifies r_{eff}-uncertainty in the fog case (not visible in the figure), while it nearly offsets it in the stratocumulus case. Note however that absorption in these two cases is negligible.

Overall uncertainty ($CRE_{065065} - CRE_{0202}$) - Mean difference = 6.2 W m^{-2}
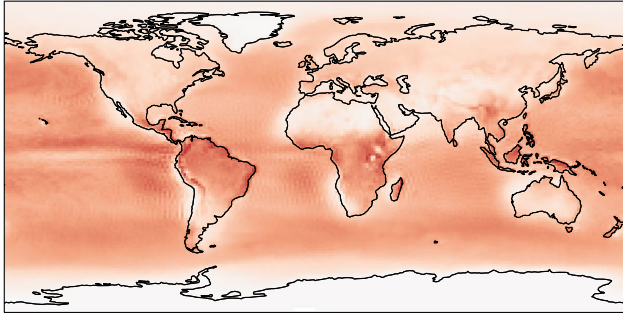
r_{eff} uncertainty ($CRE_{06502} - CRE_{0202}$) - Mean difference = 7.8 W m^{-2}
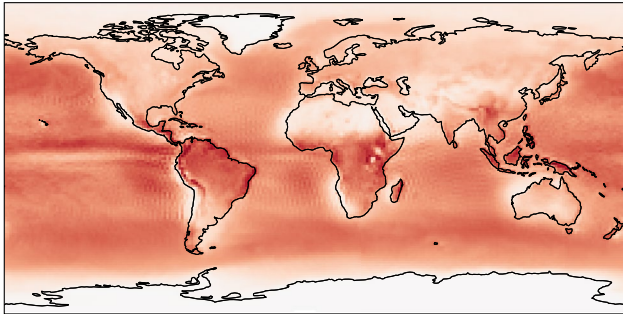
SSP uncertainty ($CRE_{065065} - CRE_{06502}$) - Mean difference = -1.6 W m^{-2}

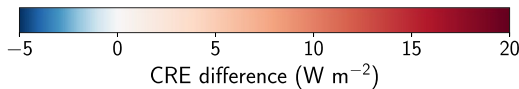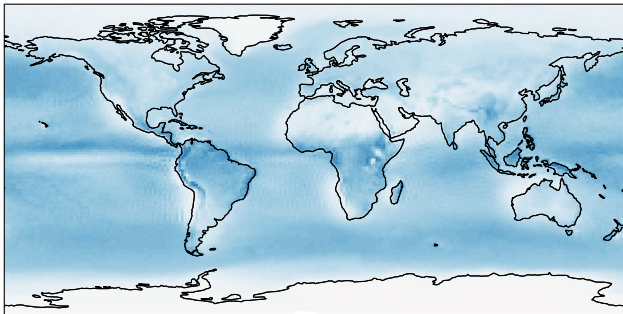

CRE difference (W m^{-2})

Figure 12. Global difference maps of the 2000–2004 average cloud radiative effect (CRE) computed from outputs of the CNRM-CM6-1 *amip* simulation for various choices of cloud single scattering properties (SSPs) and r_{eff} parameterizations. The subscripts of CRE in the titles indicate the configurations that are compared. CRE_{06502} means that k corresponding to the lognormal distribution with $\sigma = 0.65$ was used to estimate r_{eff} from the GCM LWC, and that the SSPs corresponding to the lognormal distribution with $\sigma = 0.2$ were then used.

4.3. GCM Outputs

As outlined in the introduction, CRE is a key quantity of the climate system that GCMs should correctly simulate. Although most GCMs reasonably reproduce observed SW CRE, it is such because models are tuned to match as closely as possible the observed radiative budget and SW CRE in order to avoid any drift in long-term simulations. However, simulated CRE remains very sensitive to the way clouds are treated by the radiative code. Here, the sensitivity of CRE to the parameterization of SSPs and effective radius is investigated. To this end, outputs of the CNRM-CM6-1 model are used as inputs to ecRad. TOA and surface SW fluxes in cloudy and clear-sky conditions are computed from 3-hourly full fields of the forced historical simulation *amip* (Eyring et al., 2016) performed for CMIP6 for the period 2000–2004. CRE is averaged over 5 years to compute CRE global maps, that are compared for various parameterizations, as well as their global averages. The exponential-exponential cloud overlap assumption is used in ecRad. N is computed as in Martin et al. (1994) from fixed values of cloud condensation nuclei set to 900 cm^{-3} over land and 150 cm^{-3} over sea. The effective radius is then estimated from Equation 5 with k corresponding either to $\sigma = 0.2$ or $\sigma = 0.65$. The SSPs corresponding to these two distributions are then used for both choices of k. Hence four simulations are performed. As previously this approach allows to split the r_{eff} and SSP uncertainties by comparing simulations with similar k values but different SSPs on the one hand, and distinct k but identical SSPs on the other hand. Simulations are also performed, where SSPs are consistent with k.

Figure 12 shows maps of the TOA SW CRE differences. The top panel shows the difference between the fully consistent simulations with $\sigma = 0.65$ and $\sigma = 0.2$. Differences up to 15 W m^{-2} are found in the Tropics, where low clouds dominate, and the global average differs by 6.2 W m^{-2}. The middle panel shows the r_{eff} − *uncertainty*, assuming $\sigma = 0.65$ or $\sigma = 0.2$ in Equation 5 while using only the SSPs corresponding to $\sigma = 0.2$. Differences up to 18 W m^{-2} are found in the Tropics, and the global average differs by 7.8 W m^{-2}. The bottom panel shows *SSP-uncertainty*, using the SSPs corresponding to $\sigma = 0.65$ and $\sigma = 0.2$ while using the same k corresponding to $\sigma = 0.65$. The differences do not exceed −4 W m^{-2} and the global averages differ by −1.6 W m^{-2}. Note that these differences are approximately twice larger if the more extreme value $\sigma = 0.9$ is used instead of $\sigma = 0.65$. As expected, as k decreases with σ, a wider DSD (i.e., larger σ) results in clouds with larger r_{eff} hence lower reflectance and less negative TOA CRE. On the contrary, for a given r_{eff} using the SSPs of a wider DSD intensifies the CRE. Although this second effect is one order of magnitude less than r_{eff} impact it partially offsets the main impact. It is worth comparing these numbers to the observed CRE value (−47.7 W m^{-2}) and to the range of CRE simulated by CMIP6 participating models (spread of 19.2 W m^{-2} and standard deviation of 3.6 W m^{-2}). This highlights that the impact of DSD shape is far from being negligible, and that the underlying assumptions made in different GCMs should not be overlooked when investigating differences in CRE. It also suggests that changing the underlying hypothesis on the DSD in a GCM could significantly alter its radiative budget, and consequently the tuning required to match observations. The same maps were computed for the surface and atmospheric CRE (not shown). For the surface, the global differences are very similar (6.3, 7.8 and −1.5 W m^{-2} for the overall, r_{eff}, and SSP uncertainties, respectively). For the atmospheric CRE, which is slightly positive (between 4 and 7 W m^{-2} according to Wild, 2020), the differences are of the order of 0.1 W m^{-2}, but it is worth noting that most of it is due to the choice of SSPs.

5. Conclusion and Discussion

Shortwave bulk radiative properties of liquid clouds (transmittance, reflectance and absorptance) critically depend on their optical properties at the droplet scale. The derivation of these properties in atmospheric models generally involves two steps: (a) estimating the DSD effective radius (r_{eff}) and (b) estimating the SSPs from r_{eff}. SSPs are modulated by the DSD and the frequency of incident light, two quantities that are not fully resolved in GCMs. Indeed, LWC is generally the single prognostic cloud property provided by cloud schemes and the embedded radiative code has a limited spectral resolution. For these reasons, estimating cloud optical properties implies making an assumption on the DSD and finding strategies to average the SSPs over spectral bands. This generally results in SSPs parameterizations in terms of r_{eff} for each band. This study aimed at estimating the impact of the aforementioned assumptions on the simulated SW CRE, the latter being a key characteristic of Earth climate, showing however a significant variability across GCMs. To this end we developed a new set of SSPs parameterizations that explicitly account for the shape of the DSD and cover a variety of spectral averaging methods. These parameterizations were implemented in the radiative code ecRad and offline simulations were performed on a variety of 1D cloud profiles, including idealized profiles, profiles obtained from LES and outputs from a GCM. Our results show that the assumption on the DSD significantly alters the simulated fluxes at the surface and TOA, up to several tens of W m^{-2}. Atmospheric absorption and heating rates are also affected in the case of optically thick clouds. This implies that care should be taken in DSD shape assumptions when studying the radiative impact of liquid clouds.

To quantify the uncertainty associated with the choice of the DSD, the estimation of r_{eff} and the SSPs computation were distinguished. Over the variety of clouds analyzed in this study, the r_{eff}-*uncertainty* dominates the uncertainty. The *SSP-uncertainty*, which is about five times smaller, tends to counteract the r_{eff}-uncertainty. The uncertainty resulting from spectral averaging is substantially lower but still impacts absorption, especially in clouds with large liquid water paths (LWP). This is expected as spectral averaging only impacts the estimation of the single scattering co-albedo which quantifies absorption. Note however that the radiative code used in this study has 14 bands in the SW, so that larger spectral averaging errors are expected for radiative codes with fewer bands. When applied to global outputs of a GCM, the parameterizations revealed that the SW CRE can vary by 6.2 W m^{-2} depending on the assumed DSD, which is about 13% of the measured SW CRE, with local differences up to 15 W m^{-2} over the Tropics where low clouds are ubiquitous. These differences are primarily due to the 50% difference in the estimation of r_{eff} obtained when using distinct values of k in Equation 5.

In most atmospheric models, the estimation of r_{eff}, a quantity that is only used in the radiative code, is made independently of the assumptions made in the microphysical scheme. Likewise the DSD from which SSPs parameterizations were derived is distinct from the previous ones. Our results emphasize the importance of using a consistent DSD throughout the microphysical and radiative schemes, which is practically rarely the case. Several studies have already underlined the importance of using the same DSD in the microphysical and radiative schemes. Improvements in surface radiation, precipitation and temperature were thus reported as a result of such consistent simulations with WRF (Bae et al., 2016; Thompson et al., 2016). Sieron et al. (2017) also showed that ensuring consistency altered the satellite radiances simulated from WRF model outputs. Positive impacts on temperature and CRE were also reported for the Met Office Unified Model Global Atmosphere 5.0 (GR5) (Baran et al., 2014). We are currently working on the harmonization of microphysical and radiative schemes in the Meso-NH model, which will be the focus of a future study.

This study confirms that r_{eff} is a key property and drives cloud radiative forcing. r_{eff}, as an indicator of droplet size, greatly depends on the number concentration of droplets N, which itself depends on the amount of cloud condensation nuclei. In the past, many studies focused on the relation between N and r_{eff}, in particular when investigating the indirect aerosol effect through the so-called Twomey effect (Twomey, 1974). Increased levels of aerosols tend to increase N, hence to reduce r_{eff}, making clouds brighter and cooling the Earth system. However we have demonstrated that for a given LWC, r_{eff} also depends on the parameter k which is directly related to the DSD shape and can vary by a factor of 6 based on observations. From the introduction of this k parameter by Pontikis and Hicks (1992), many GCMs have used constant k values to describe very different clouds. For instance, $k = 0.36$ in CanAM4 (Von Salzen et al., 2013), $k = 0.75$ in the IPSL (Madeleine et al., 2020) and CN-RM-CM6-1 (Roehrig et al., 2020) climate models. In ECHAM6 (Stevens et al., 2013) $k = 0.67$ over land and $k = 0.8$ over ocean, as proposed by Martin et al. (1994). It shows that the CRE computed from these models would greatly differ even if LWC and N were strictly similar. Several theoretical studies (Liu et al., 2008; Igel &

van den Heever, 2017; M. Wang et al., 2020) reported correlations between k, N, microphysical processes (e.g., autoconversion and evaporation) and dynamics (e.g., vertical velocity). They tried to quantify the radiative effect of such correlations on the indirect aerosol effect. Rotstayn and Liu (2003, 2009) and W. Zhao et al. (2018) have shown the advantages of considering such a correlation in climate models. Some observation-based studies, on the contrary, reject the general relation between N and k (Brenguier et al., 2011; Tas et al., 2015; Y. Wang et al., 2021). This overall highlights that k remains a very poorly constrained parameter which would deserve more investigation and a detailed parameterization in GCMs.

To conclude, attention must be put on two aspects. First, given the crucial importance of k in the CRE uncertainty deduced from the results of the present study, explicitly relating k to the physics of the model, instead of using a fixed value for all clouds, appears as a priority. Second, in the mentioned studies which investigated the effect of k on indirect aerosol effect, only the r_{eff}-*uncertainty* was considered, the *SSPs-uncertainty* being ignored while the present study has demonstrated its own significance. Our fully consistent parameterizations, accounting for the impact of DSD both on the estimation of r_{eff} and on the SSPs, thus provide a more robust framework for reliable studies of the indirect aerosol radiative effect. Finally it is worth bearing in mind that this study was restricted to the SW impact of liquid clouds. To have a global picture of the impact of DSD assumptions on CRE, it should be extended to ice clouds and to the longwave.

Appendix A: Two-Stream Approximation

To compute the bulk radiative properties of a cloud layer, the plane-parallel radiative transfer equation must be solved. A widely used solution, especially in fast radiative codes used in NWP and climate models, is the two-stream approximation. It can provide analytical expressions for reflectance and transmittance of the layer under diffuse and direct illumination, given the asymmetry parameter g, optical thickness τ and single scattering albedo ω. Using the δ-Eddington approximation (Joseph et al., 1976) and the approach of Aquíno and Varela (2005), transmittance and reflectance for a homogeneous cloud layer can be written as:

$$T = \frac{\Gamma K_1 e^{\kappa\tau} + K_2 e^{-\kappa\tau} + G^- e^{-\tau/\mu_0} + F_0 \mu_0 e^{-\tau/\mu_0}}{F_0 \mu_0}, \tag{A1}$$

$$R = \frac{K_1 + \Gamma K_2 + G^+}{F_0 \mu_0}, \tag{A2}$$

where the spectral dependence is omitted for sake of simplicity. The irradiance impinging on the top of the cloud is denoted with $F_0 \mu_0$, μ_0 being the cosine of the solar zenith angle (θ_0). The latter expressions hence correspond to direct illumination. This avoids the unrealistic negative values which can be obtained under diffuse illumination (Wiscombe, 1977). θ_0 was fixed to 50° which corresponds to standard illumination conditions. The parameters in Equations A1 and A2 are given by:

$$K_1 = \frac{\Gamma G^- e^{-\kappa\tau^*} - G^+ e^{-\tau^*/\mu_0}}{e^{\kappa\tau^*} - \Gamma^2 e^{-\kappa\tau^*}} \tag{A3}$$

$$K_2 = -(G^- + \Gamma K_1) \tag{A4}$$

$$G^- = \frac{\mu_0^2 \omega F_0}{(\kappa\mu_0)^2 - 1} \left[\left(\gamma_1 + \frac{1}{\mu_0}\right)\gamma_4 + \gamma_2\gamma_3\right] \tag{A5}$$

$$G^+ = \frac{\mu_0^2 \omega F_0}{(\kappa\mu_0)^2 - 1} \left[\left(\gamma_1 - \frac{1}{\mu_0}\right)\gamma_3 + \gamma_2\gamma_4\right] \tag{A6}$$

$$\gamma_1 = \frac{1}{4}[7 - \omega^*(4 + 3g^*)], \qquad \gamma_2 = -\frac{1}{4}[1 - \omega^*(4 - 3g^*)], \tag{A7}$$

$$\gamma_3 = \frac{1}{4}(2 - 3g^*\mu_0), \qquad \gamma_4 = \frac{1}{4}(2 + 3g^*\mu_0), \tag{A8}$$

$$\kappa = \sqrt{\gamma_1{}^2 - \gamma_2{}^2}, \tag{A9}$$

$$\Gamma = \frac{\gamma_1 - \kappa}{\gamma_2}. \tag{A10}$$

and * refers to the δ-scaling such that:

$$g^* = \frac{1}{g+1}, \qquad \tau^* = (1 - \omega f)\tau, \qquad \omega^* = \frac{(1-f)\omega}{1 - \omega f}. \tag{A11}$$

For the development of the SSPs parameterizations, the value of τ generally corresponds to the wavelength of 0.55 μm. $\tau(\lambda)$ can be computed from the extinction efficiency $Q_{\text{ext}}(\lambda)$:

$$\tau(\lambda) = \tau(0.55)\frac{Q_{\text{ext}}(\lambda)}{Q_{\text{ext}}(0.55)}. \tag{A12}$$

Data Availability Statement

The parameterizations coefficients and the reference values of SSPs are available in: https://github.com/erfanjhn/liq-cloud-opt-param.git. The experiments of CMIP-6 CNRM-CM6-1 are made available via the portal: https://esgf-node.llnl.gov/search/cmip6.

References

Ahlgrimm, M., Forbes, R. M., Hogan, R. J., & Sandu, I. (2018). Understanding global model systematic shortwave radiation errors in subtropical marine boundary layer cloud regimes. *Journal of Advances in Modeling Earth Systems*, *10*(8), 2042–2060. https://doi.org/10.1029/2018MS001346

Aquíno, J., & Varela, J. (2005). Two stream approximation to radiative transfer equation: An alternative method of solution. *Revista Mexicana de Física*, *51*, 82–86.

Bae, S. Y., Hong, S.-Y., & Lim, K.-S. S. (2016). Coupling WRF double-moment 6-class microphysics schemes to RRTMG radiation scheme in weather research forecasting model. *Advances in Meteorology*, *2016*, 1–11. https://doi.org/10.1155/2016/5070154

Baran, A. J., Hill, P., Furtado, K., Field, P., & Manners, J. (2014). A coupled cloud physics–radiation parameterization of the bulk optical properties of cirrus and its impact on the Met Office Unified Model Global Atmosphere 5.0 configuration. *Journal of Climate*, *27*(20), 7725–7752. https://doi.org/10.1175/JCLI-D-13-00700.1

Barker, H. W., Cole, J. N. S., Li, J., & von Salzen, K. (2016). A parametrization of 3-D subgrid-scale clouds for conventional GCMs: Assessment using A-Train satellite data and solar radiative transfer characteristics. *Journal of Advances in Modeling Earth Systems*, *8*(2), 566–597. https://doi.org/10.1002/2015MS000601

Barker, H. W., Pincus, R., & Morcrette, J. J. (2002). The Monte Carlo independent column approximation: Application within large-scale models. In *Proceedings of the gcss/arm workshop on the representation of cloud systems in large-scale models*.

Baum, B. A., Yang, P., Heymsfield, A. J., Schmitt, C. G., Xie, Y., Bansemer, A., & Zhang, Z. (2011). Improvements in shortwave bulk scattering and absorption models for the remote sensing of ice clouds. *Journal of Applied Meteorology and Climatology*, *50*(5), 1037–1056. https://doi.org/10.1175/2010JAMC2608.1

Boucher, O., & Lohmann, U. (1995). The sulfate-CCN-cloud albedo effect. *Tellus B: Chemical and Physical Meteorology*, *47*(3), 281–300. https://doi.org/10.1034/j.1600-0889.47.issue3.1.x

Brenguier, J. L., Burnet, F., & Geoffroy, O. (2011). Cloud optical thickness and liquid water path-does the k coefficient vary with droplet concentration? *Atmospheric Chemistry and Physics*, *11*(18), 9771–9786. https://doi.org/10.5194/acp-11-9771-2011

Brenguier, J.-L., Pawlowska, H., Schüller, L., Preusker, R., Fischer, J., & Fouquart, Y. (2000). Radiative properties of boundary layer clouds: Droplet effective radius versus number concentration. *Journal of the Atmospheric Sciences*, *57*(6), 803–821. https://doi.org/10.1175/1520-0469(2000)057<0803:RPOBLC>2.0.CO;2

Brient, F., Couvreux, F., Villefranque, N., Rio, C., & Honnert, R. (2019). Object-oriented identification of coherent structures in large Eddy simulations: Importance of downdrafts in stratocumulus. *Geophysical Research Letters*, *46*(5), 2854–2864. https://doi.org/10.1029/2018GL081499

Brown, A. R., Cederwall, R. T., Chlond, A., Duynkerke, P. G., Golaz, J. C., Khairoutdinov, M., et al. (2002). Large-eddy simulation of the diurnal cycle of shallow cumulus convection over land. *Quarterly Journal of the Royal Meteorological Society*, *128*, 1075–1093. https://doi.org/10.1256/003590002320373210

Cahalan, R. F., Oreopoulos, L., Marshak, A., Evans, K. F., Davis, A. B., Pincus, R., et al. (2005). The 13RC: Bringing together the most advanced radiative transfer tools for cloudy atmospheres. *Bulletin of the American Meteorological Society*, *86*(9), 1275–1294. https://doi.org/10.1175/BAMS-86-9-1275

Charlock, T. P., & Ramanathan, V. (1985). The Albedo field and cloud radiative forcing produced by a general circulation model with internally generated cloud optics. *Journal of the Atmospheric Sciences*, *42*(13), 1408–1429. https://doi.org/10.1175/1520-0469(1985)042<1408:tafacr>2.0.co;2

Chou, M.-D., Suarez, M. J., Ho, C.-H., Yan, M. M.-H., & Lee, K.-T. (1998). Parameterizations for cloud overlapping and shortwave single-scattering properties for use in general circulation and cloud ensemble models. *Journal of Climate*, *11*(2), 202–214. https://doi.org/10.1175/1520-0442(1998)011<0202:PFCOAS>2.0.CO;2

Clough, S. A., Shephard, M. W., Mlawer, E. J., Delamere, J. S., Iacono, M. J., Cady-Pereira, K., & Brown, P. D. (2005). Atmospheric radiative transfer modeling: A summary of the AER codes. *Journal of Quantitative Spectroscopy and Radiative Transfer*, *91*(2), 233–244. https://doi.org/10.1016/j.jqsrt.2004.05.058

Costa, S., & Shine, K. (2006). An estimate of the global impact of multiple scattering by clouds on outgoing long-wave radiation. *Quarterly Journal of the Royal Meteorological Society*, *132*(616), 885–895. https://doi.org/10.1256/qj.05.169

Di Giuseppe, F., & Tompkins, A. M. (2015). Generalizing cloud overlap treatment to include the effect of wind shear. *Journal of the Atmospheric Sciences*, *72*(8), 2865–2876. https://doi.org/10.1175/JAS-D-14-0277.1

Dobbie, J. S., Li, J., & Chýlek, P. (1999). Two-and four-stream optical properties for water clouds and solar wavelengths. *Journal of Geophysical Research*, *104*(D2), 2067–2079. https://doi.org/10.1029/1998jd200039

Ducongé, L. (2019). *Étude du cycle de vie du brouillard radiatif durant la campagne LANFEX: Impact de la dynamique en terrain vallonné et des processus microphysiques*. Unpublished doctoral dissertation. University of Toulouse.

Dudhia, J. (1989). Numerical study of convection observed during the winter monsoon experiment using a mesoscale two-dimensional model. *Journal of the Atmospheric Sciences*, *46*(20), 3077–3107. https://doi.org/10.1175/1520-0469(1989)046<3077:NSOCOD>2.0.CO;2

Duynkerke, P. G., de Roode, S. R., van Zanten, M. C., Calvo, J., Cuxart, J., Cheinet, S., et al. (2004). Observations and numerical simulations of the diurnal cycle of the EUROCS stratocumulus case. *Quarterly Journal of the Royal Meteorological Society*, *130C*(604), 3269–3296. https://doi.org/10.1256/qj.03.139

Edwards, J. M., Havemann, S., Thelen, J.-C., & Baran, A. J. (2007). A new parametrization for the radiative properties of ice crystals: Comparison with existing schemes and impact in a GCM. *Atmospheric Research*, *83*(1), 19–35. https://doi.org/10.1016/j.atmosres.2006.03.002

Edwards, J. M., & Slingo, A. (1996). Studies with a flexible new radiation code. I: Choosing a configuration for a large-scale model. *Quarterly Journal of the Royal Meteorological Society*, *122*(531), 689–719. https://doi.org/10.1002/qj.49712253107

Engström, A., Bender, F. A., & Karlsson, J. (2014). Improved representation of marine stratocumulus cloud shortwave radiative properties in the CMIP5 climate models. *Journal of Climate*, *27*(16), 6175–6188. https://doi.org/10.1175/JCLI-D-13-00755.1

Espinoza, R. C., Jr. (1996). Parameterization of solar near-infrared radiative properties of cloudy layers. *Journal of the Atmospheric Sciences*, *53*(11), 1559–1568. https://doi.org/10.1175/1520-0469(1996)053<1559:POSNIR>2.0.CO;2

Eyring, V., Bony, S., Meehl, G. A., Senior, C. A., Stevens, B., Stouffer, R. J., & Taylor, K. E. (2016). Overview of the Coupled Model Intercomparison Project Phase 6 (CMIP6) experimental design and organization. *Geoscientific Model Development*, *9*(5), 1937–1958. https://doi.org/10.5194/gmd-9-1937-2016

Fouquart, Y. (1988). Radiative transfer in climate models. In *Physically-based modelling and simulation of climate and climatic change* (pp. 223–283). Springer. https://doi.org/10.1007/978-94-009-3041-4_5

Fouquart, Y., & Bonnel, B. (1980). Computations of solar heating of the earth's atmosphere: A new parameterization. *Beiträge zur Physik der Atmosphäre*, *53*.

Fouquart, Y., Bonnel, B., & Ramaswamy, V. (1991). Intercomparing shortwave radiation codes for climate studies. *Journal of Geophysical Research*, *96*(D5), 8955–8968. https://doi.org/10.1029/90jd00290

Freidenreich, S. M., & Ramaswamy, V. (2005). Refinement of the Geophysical Fluid Dynamics Laboratory solar benchmark computations and an improved parameterization for climate models. *Journal of Geophysical Research*, *110*(D17), D17105. https://doi.org/10.1029/2004JD005471

Geleyn, J. F., JF, G., & Others. (1979). An economical analytical method for the computation of the interaction between scattering and line absorption of radiation. *Beiträge zur Physik der Atmosphäre*, *52*(1), 1–16.

Geleyn, J. F., Mašek, J., Brožková, R., Kuma, P., Degrauwe, D., Hello, G., & Pristov, N. (2017). Single interval longwave radiation scheme based on the net exchanged rate decomposition with bracketing. *Quarterly Journal of the Royal Meteorological Society*, *143*(704), 1313–1335. https://doi.org/10.1002/qj.3006

Geoffroy, O., Brenguier, J. L., & Burnet, F. (2010). Parametric representation of the cloud droplet spectra for les warm bulk microphysical schemes. *Atmospheric Chemistry and Physics*, *10*(10), 4835–4848. https://doi.org/10.5194/acp-10-4835-2010

Grenfell, T. C., & Warren, S. G. (1999). Representation of a nonspherical ice particle by a collection of independent spheres for scattering and absorption of radiation. *Journal of Geophysical Research*, *104*(D24), 31697–31709. https://doi.org/10.1029/1999JD900496

Hale, G. M., & Querry, M. R. (1973). Optical constants of water in the 200-nm to 200-μm wavelength region. *Applied Optics*, *12*(3), 555–563. https://doi.org/10.1364/AO.12.000555

Hansen, J. E. (1971). Multiple scattering of polarized light in planetary atmospheres part II. Sunlight reflected by terrestrial water clouds. *Journal of the Atmospheric Sciences*, *28*(8), 1400–1426. https://doi.org/10.1175/1520-0469(1971)028<1400:MSOPLI>2.0.CO;2

Hogan, R. J., & Bozzo, A. (2018). A flexible and efficient radiation scheme for the ECMWF model. *Journal of Advances in Modeling Earth Systems*, *10*(8), 1990–2008. https://doi.org/10.1029/2018MS001364

Hogan, R. J., & Illingworth, A. J. (2000). Deriving cloud overlap statistics from radar. *Quarterly Journal of the Royal Meteorological Society*, *126*(569). https://doi.org/10.1002/qj.49712656914

Hogan, R. J., Schäfer, S. A. K., Klinger, C., Chiu, J. C., & Mayer, B. (2016). Representing 3-D cloud radiation effects in two-stream schemes: 2. Matrix formulation and broadband evaluation. *Journal of Geophysical Research: Atmospheres*, *121*(14), 8583–8599. https://doi.org/10.1002/2016jd024875

Hourdin, F., Foujols, M. A., Codron, F., Guemas, V., Dufresne, J. L., Bony, S., & Bopp, L. (2013). Impact of the LMDZ atmospheric grid configuration on the climate and sensitivity of the IPSL-CM5A coupled model. *Climate Dynamics*, *40*(9–10), 2167–2192. https://doi.org/10.1007/s00382-012-1411-3

Hu, Y., & Stamnes, K. (1993). An accurate parameterization of the radiative properties of water clouds suitable for use in climate models. *Journal of Climate*, *6*(4), 728–742. https://doi.org/10.1175/1520-0442(1993)006<0728:aapotr>2.0.co;2

Hu, Y., & Stamnes, K. (2000). Climate sensitivity to cloud optical properties. *Tellus Series B Chemical and Physical Meteorology*, *52*(1), 81–93. https://doi.org/10.3402/tellusb.v52i1.16084

Igel, A. L., & van den Heever, S. C. (2017). The importance of the shape of cloud droplet size distributions in shallow cumulus clouds. Part II: Bulk microphysics simulations. *Journal of the Atmospheric Sciences*, *74*(1), 259–273. https://doi.org/10.1175/jas-d-15-0383.1

Joseph, J. H., Wiscombe, W. J., & Weinman, J. A. (1976). The delta-Eddington approximation for radiative flux transfer. *Journal of the Atmospheric Sciences*, *33*(12), 2452–2459. https://doi.org/10.1175/1520-0469(1976)033<2452:TDEAFR>2.0.CO;2

Jouhaud, J., Dufresne, J. L., Madeleine, J. B., Hourdin, F., Couvreux, F., Villefranque, N., & Jam, A. (2018). Accounting for vertical subgrid-scale heterogeneity in low-level cloud fraction parameterizations. *Journal of Advances in Modeling Earth Systems*, *10*(11), 2686–2705. https://doi.org/10.1029/2018MS001379

Kurucz, R. L. (1994). Synthetic infrared spectra. *Symposium - International Astronomical Union*, *154*, 523–531. https://doi.org/10.1017/S0074180900124805

Lac, C., Chaboureau, J.-P., Masson, V., Pinty, J.-P., Tulet, P., Escobar, J., et al. (2018). Overview of the Meso-NH model version 5.4 and its applications. *Geoscientific Model Development*, *11*(5), 1929–1969. https://doi.org/10.5194/gmd-11-1929-2018

Liu, Y., Daum, P. H., Guo, H., & Peng, Y. (2008). Dispersion bias, dispersion effect, and the aerosol–cloud conundrum. *Environmental Research Letters*, *3*(4), 45021. https://doi.org/10.1088/1748-9326/3/4/045021

Loeb, N. G., Doelling, D. R., Wang, H., Su, W., Nguyen, C., Corbett, J. G., et al. (2018). Clouds and the Earth's radiant energy system (CERES) energy balanced and filled (EBAF) top-of-atmosphere (TOA) edition-4.0 data product. *Journal of Climate*, *31*(2), 895–918. https://doi.org/10.1175/JCLI-D-17-0208.1

Lu, P., Zhang, H., & Li, J. (2011). Correlated k-distribution treatment of cloud optical properties and related radiative impact. *Journal of the Atmospheric Sciences*, *68*(11), 2671–2688. https://doi.org/10.1175/jas-d-10-05001.1

Madeleine, J. B., Hourdin, F., Grandpeix, J. Y., Rio, C., Dufresne, J. L., Vignon, E., et al. (2020). Improved representation of clouds in the atmospheric component LMDZ6A of the IPSL-CM6A Earth system model. *Journal of Advances in Modeling Earth Systems*, *12*(10), e2020MS002046. https://doi.org/10.1029/2020MS002046

Manners, J. (2015). Socrates technical guide suite of community radiative transfer codes based on edwards and slingo. In *Tech. rep*. Met Office.

Martin, G. M., Johnson, D. W., & Spice, A. (1994). The measurement and parameterization of effective radius of droplets in warm stratocumulus clouds. *Journal of the Atmospheric Sciences*, *51*(13), 1823–1842. https://doi.org/10.1175/1520-0469(1994)051<1823:tmapoe>2.0.co;2

Mätzler, C. (2002). *MATLAB functions for Mie scattering and absorption, version 2*. IAP Res. Rep (Vol. 8, p. 9).

Meador, W. E., & Weaver, W. R. (1980). Two-stream approximations to radiative transfer in planetary atmospheres: A unified description of existing methods and a new improvement. *Journal of the Atmospheric Sciences*, *37*(3), 630–643. https://doi.org/10.1175/1520-0469(1980)037<0630:TSATRT>2.0.CO;2

Miles, N. L., Verlinde, J., & Clothiaux, E. E. (2000). Cloud droplet size distributions in low-level stratiform clouds. *Journal of the Atmospheric Sciences*, *57*(2), 295–311. https://doi.org/10.1175/1520-0469(2000)057<0295:CDSDIL>2.0.CO;2

Mishchenko, M. I., Dlugach, J. M., Yanovitskij, E. G., & Zakharova, N. T. (1999). Bidirectional reflectance of flat, optically thick particulate layers: An efficient radiative transfer solution and applications to snow and soil surfaces. *Journal of Quantitative Spectroscopy and Radiative Transfer*, *63*(2–6), 409–432. https://doi.org/10.1016/S0022-4073(99)00028-X

Misumi, R., Uji, Y., Tobo, Y., Miura, K., Uetake, J., Iwamoto, Y., et al. (2018). Characteristics of droplet size distributions in low-level stratiform clouds observed from Tokyo Skytree. *Journal of the Meteorological Society of Japan. Ser. II*, *96*(4), 405–413. https://doi.org/10.2151/jmsj.2018-040

Mitchell, D. L. (2002). Effective diameter in radiation transfer: General definition, applications, and limitations. *Journal of the Atmospheric Sciences*, *59*(15), 2330–2346. https://doi.org/10.1175/1520-0469(2002)059<2330:EDIRTG>2.0.CO;2

Mlawer, E. J., Taubman, S. J., Brown, P. D., Iacono, M. J., & Clough, S. A. (1997). Radiative transfer for inhomogeneous atmospheres: RRTM, a validated correlated-k model for the longwave. *Journal of Geophysical Research*, *102*(D14), 16663–16682. https://doi.org/10.1029/97JD00237

Morcrette, J. J., Barker, H. W., Cole, J. N., Iacono, M. J., & Pincus, R. (2008). Impact of a new radiation package, McRad, in the ECMWF integrated forecasting system. *Monthly Weather Review*, *136*(12), 4773–4798. https://doi.org/10.1175/2008MWR2363.1

Nam, C., Bony, S., Dufresne, J.-L., & Chepfer, H. (2012). The 'too few, too bright' tropical low-cloud problem in CMIP5 models. *Geophysical Research Letters*, *39*(21), L21801. https://doi.org/10.1029/2012GL053421

Nielsen, K. P., Gleeson, E., & Rontu, L. (2014). Radiation sensitivity tests of the HARMONIE 37h1 NWP model. *Geoscientific Model Development*, *7*(4), 1433–1449. https://doi.org/10.5194/gmd-7-1433-2014

Pincus, R., Barker, H. W., & Morcrette, J.-J. (2003). A fast, flexible, approximate technique for computing radiative transfer in inhomogeneous cloud fields. *Journal of Geophysical Research*, *108*(D13), 4376. https://doi.org/10.1029/2002JD003322

Pincus, R., Hannay, C., Klein, S. A., Xu, K.-M., & Hemler, R. (2005). Overlap assumptions for assumed probability distribution function cloud schemes in large-scale models. *Journal of Geophysical Research*, *110*(D15), D15S09. https://doi.org/10.1029/2004jd005100

Pontikis, C., & Hicks, E. (1992). Contribution to the cloud droplet effective radius parameterization. *Geophysical Research Letters*, *19*(22), 2227–2230. https://doi.org/10.1029/92gl02283

Pope, V., Gallani, M., Rowntree, P., & Stratton, R. A. (2000). The impact of new physical parametrizations in the Hadley centre climate model: HadAM3. *Climate Dynamics*, *16*, 123–146. https://doi.org/10.1007/s003820050009

Price, J. D., Lane, S., Boutle, I. A., Smith, D. K., Bergot, T., Lac, C., et al. (2018). LANFEX: A field and modeling study to improve our understanding and forecasting of radiation fog. *Bulletin of the American Meteorological Society*, *99*(10), 2061–2077. https://doi.org/10.1175/BAMS-D-16-0299.1

Räisänen, P. (1999). Parameterization of water and ice cloud near-infrared single-scattering co-albedo in broadband radiation schemes. *Journal of the Atmospheric Sciences*, *56*(4), 626–641. https://doi.org/10.1175/1520-0469(1999)056<0626:powaic>2.0.co;2

Räisänen, P., Barker, H. W., Khairoutdinov, M. F., Li, J., & Randall, D. A. (2004). Stochastic generation of subgrid-scale cloudy columns for large-scale models. *Quarterly Journal of the Royal Meteorological Society*, *130*(601), 2047–2067. https://doi.org/10.1256/qj.03.99

Ritter, B., & Geleyn, J.-F. (1992). A comprehensive radiation scheme for numerical weather prediction models with potential applications in climate simulations. *Monthly Weather Review*, *120*(2), 303–325. https://doi.org/10.1175/1520-0493(1992)120<0303:acrsfn>2.0.co;2

Roehrig, R., Beau, I., Saint-Martin, D., Alias, A., Decharme, B., Guérémy, J. F., et al. (2020). The CNRM global atmosphere model ARPEGE-Climat 6.3: Description and evaluation. *Journal of Advances in Modeling Earth Systems*, *12*(7), e2020MS002075. https://doi.org/10.1029/2020MS002075

Rotstayn, L. D., & Liu, Y. (2003). Sensitivity of the first indirect aerosol effect to an increase of cloud droplet spectral dispersion with droplet number concentration. *Journal of Climate*, *16*(21), 3476–3481. https://doi.org/10.1175/1520-0442(2003)016<3476:SOTFIA>2.0.CO;2

Rotstayn, L. D., & Liu, Y. (2009). Cloud droplet spectral dispersion and the indirect aerosol effect: Comparison of two treatments in a GCM. *Geophysical Research Letters*, *36*(10), L10801. https://doi.org/10.1029/2009GL038216

Shonk, J. K. P., & Hogan, R. J. (2008). Tripleclouds: An efficient method for representing horizontal cloud inhomogeneity in 1D Radiation schemes by using three regions at each height. *Journal of Climate*, *21*(11), 2352–2370. https://doi.org/10.1175/2007JCLI1940.1

Sieron, S. B., Clothiaux, E. E., Zhang, F., Lu, Y., & Otkin, J. A. (2017). Comparison of using distribution-specific versus effective radius methods for hydrometeor single-scattering properties for all-sky microwave satellite radiance simulations with different microphysics parameterization schemes. *Journal of Geophysical Research*, *122*(13), 7027–7046. https://doi.org/10.1002/2017JD026494

Slingo, A., & Schrecker, H. M. (1982). On the shortwave radiative properties of stratiform water clouds. *Quarterly Journal of the Royal Meteorological Society*, *108*(456), 407–426. https://doi.org/10.1002/qj.49710845607

Stephens, G. L. (1978). Radiation profiles in extended water clouds. II: Parameterization schemes. *Journal of the Atmospheric Sciences*, *35*, 2123–2132. https://doi.org/10.1175/1520-0469(1978)035<2123:rpiewc>2.0.co;2

Stevens, B., Giorgetta, M., Esch, M., Mauritsen, T., Crueger, T., Rast, S., et al. (2013). Atmospheric component of the mpi-m earth system model: Echam6. *Journal of Advances in Modeling Earth Systems*, *5*(2), 146–172. https://doi.org/10.1002/jame.20015

Strauss, C. (2020). *Quelle turbulence sur les bords des nuages convectifs?* Unpublished doctoral dissertation. University of Toulouse.

Sulak, A. M., Calabrase, W. J., Ryan, S. D., & Heus, T. (2020). The contributions of shear and turbulence to cloud overlap for cumulus clouds. *Journal of Geophysical Research: Atmospheres*, *125*(10), e2019JD032017. https://doi.org/10.1029/2019JD032017

Tas, E., Teller, A., Altaratz, O., Axisa, D., Bruintjes, R., Levin, Z., & Koren, I. (2015). The relative dispersion of cloud droplets: Its robustness with respect to key cloud properties. *Atmospheric Chemistry and Physics*, *15*(4), 2009–2017. https://doi.org/10.5194/acp-15-2009-2015

Thompson, G., Tewari, M., Ikeda, K., Tessendorf, S., Weeks, C., Otkin, J., & Kong, F. (2016). Explicitly-coupled cloud physics and radiation parameterizations and subsequent evaluation in wrf high-resolution convective forecasts. *Atmospheric Research*, *168*, 92–104. https://doi.org/10.1016/j.atmosres.2015.09.005

Twomey, S. (1974). Pollution and the planetary albedo. *Atmospheric Environment (1967)*, *8*(12), 1251–1256. https://doi.org/10.1016/0004-6981(74)90004-3

Van De Hulst, H. C. (1968). Radiative transfer in thick atmospheres with an arbitrary scattering function. *Bulletin of the Astronomical Institutes of the Netherlands*, *20*, 77–86.

Vié, B., Pinty, J.-P., Berthet, S., & Leriche, M. (2016). LIMA (v1.0): A quasi two-moment microphysical scheme driven by a multimodal population of cloud condensation and ice freezing nuclei. *Geoscientific Model Development*, *9*(2), 567–586. https://doi.org/10.5194/gmd-9-567-2016

Vignesh, P. P., Jiang, J. H., Kishore, P., Su, H., Smay, T., Brighton, N., & Velicogna, I. (2020). Assessment of cmip6 cloud fraction and comparison with satellite observations. *Earth and Space Science*, *7*(2), e2019EA000975. https://doi.org/10.1029/2019ea000975

Voldoire, A., Saint-Martin, D., Sénési, S., Decharme, B., Alias, A., Chevallier, M., et al. (2019). Evaluation of CMIP6 DECK experiments with CNRM-CM6-1. *Journal of Advances in Modeling Earth Systems*, *11*(7), 2177–2213. https://doi.org/10.1029/2019MS001683

Von Salzen, K., Scinocca, J. F., McFarlane, N. A., Li, J., Cole, J. N. S., Plummer, D., et al. (2013). The Canadian fourth generation atmospheric global climate model (CanAM4). Part I: Representation of physical processes. *Atmosphere - Ocean*, *51*(1), 104–125. https://doi.org/10.1080/07055900.2012.755610

Wang, M., Peng, Y., Liu, Y., Liu, Y., Xie, X., & Guo, Z. (2020). Understanding cloud droplet spectral dispersion effect using empirical and semi-analytical parameterizations in NCAR CAM5.3. *Earth and Space Science*, *7*(8), e2020EA001276. https://doi.org/10.1029/2020EA001276

Wang, Y., Zhao, C., McFarquhar, G. M., Wu, W., Reeves, M., & Li, J. (2021). Dispersion of droplet size distributions in supercooled non-precipitating stratocumulus from aircraft observations obtained during the southern ocean cloud radiation aerosol transport experimental study. *Journal of Geophysical Research: Atmospheres*, *126*(6), e2020JD033720. https://doi.org/10.1029/2020JD033720

Wild, M. (2020). The global energy balance as represented in CMIP6 climate models. *Climate Dynamics*, *55*(3–4), 553–577. https://doi.org/10.1007/s00382-020-05282-7

Wild, M., Hakuba, M. Z., Folini, D., Dörig-Ott, P., Schär, C., Kato, S., & Long, C. N. (2019). The cloud-free global energy balance and inferred cloud radiative effects: An assessment based on direct observations and climate models. *Climate Dynamics*, *52*(7–8). https://doi.org/10.1007/s00382-018-4413-y

Wiscombe, W. J. (1977). The Delta–M method: Rapid yet accurate radiative flux calculations for strongly asymmetric phase functions. *Journal of the Atmospheric Sciences*, *34*(9), 1408–1422. https://doi.org/10.1175/1520-0469(1977)034<1408:tdmrya>2.0.co;2

Xu, L.-S., Zhang, G.-T., & Cheng, H.-B. (1996). Parameterization of the shortwave radiative properties of water clouds for use in GCMs. *Theoretical and Applied Climatology*, *55*(1–4), 211–219. https://doi.org/10.1007/BF00864717

Yang, P., Bi, L., Baum, B. A., Liou, K.-N., Kattawar, G. W., Mischenko, M. I., & Cole, B. (2013). Spectrally consistent scattering, absorption, and polarization properties of atmospheric ice crystals at wavelengths from 0.2 to 100 μ m. *Journal of the Atmospheric Sciences*, *70*(1), 330–347. https://doi.org/10.1175/jas-d-12-039.1

Zelinka, M. D., Myers, T. A., McCoy, D. T., Po-Chedley, S., Caldwell, P. M., Ceppi, P., & Taylor, K. E. (2020). Causes of Higher Climate Sensitivity in CMIP6 Models. *Geophysical Research Letters*, *47*(1), e2019GL085782. https://doi.org/10.1029/2019GL085782

Zhao, C., Tie, X., Brasseur, G., Noone, K. J., Nakajima, T., Zhang, Q., et al. (2006). Aircraft measurements of cloud droplet spectral dispersion and implications for indirect aerosol radiative forcing. *Geophysical Research Letters*, *33*(16), L16809. https://doi.org/10.1029/2006GL026653

Zhao, W., Peng, Y., Wang, B., Yi, B., Lin, Y., & Li, J. (2018). Comparison of three ice cloud optical schemes in climate simulations with community atmospheric model version 5. *Atmospheric Research*, *204*, 37–53. https://doi.org/10.1016/j.atmosres.2018.01.004